AIMS Mathematics, 11(6): 15524–15560.
DOI: 10.3934/math.2026639
Received: 13 March 2026
Revised: 20 May 2026
Accepted: 21 May 2026
Published: 02 June 2026

https://www.aimspress.com/journal/Math

Research article

A method of urban airspace evaluation based on availability quantification and multi-risk assessment for UAV operations

Hao Li[1], Hua Wu[1,*], Yang Liu[1,2,*], HaiLong Dong[1], HuaYu Liu[1] and Shuai Fan[1]

[1] School of Information Science & Electrical Engineering, Shandong Jiaotong University, Jinan 250357, Shandong, China

[2] Engineering Research Center of Intelligent Air-Ground Integration Vehicle and Control, Xihua University, Ministry of Education, Chengdu 610039, Sichuan, China

* **Correspondence:** Email: wuhua@sdjtu.edu.cn; liuyang@sdjtu.edu.cn.

Abstract: The application of unmanned aerial vehicles (UAVs) in urban areas enhances daily life convenience, but managing low-altitude urban airspace and mission planning remains challenging. This paper proposes a time-varying evaluation method for urban airspace management, combining airspace availability quantification and multi-risk assessment. First, a voxel-based measurement method was developed to quantify airspace availability by defining airspace coverage. Then, two risk assessment models were built: a static risk model and a dynamic risk model. The static risk model considers data transmission, collisions, indirect fatalities, and property damage; the dynamic risk model accurately quantifies direct fatalities and societal impact risks. Next, by integrating quadrant analysis with an improved Pareto ranking method, urban airspace below 40 meters was modeled and evaluated. Finally, a 3D urban airspace map with a resolution of $500 \times 500 \times 10$ was generated, and airspace connectivity tests were conducted at 10:00 A.M. and 10:00 P.M. The results show that airspace connectivity is optimal between 28 meters and 40 meters at 10:00 P.M., improving with increased altitude.

Keywords: urban airspace evaluation; availability quantification; multi-risk assessment
Mathematics Subject Classification: 90B25, 90B50

1. Introduction

The applications of unmanned aerial vehicles (UAVs) in cities are rapidly increasing [1], yet safe operations in complex urban environments remain challenging. Urban low-altitude UAV operations are constrained not only by static obstacles such as dense buildings but also by dynamic obstacles such as spatiotemporal population flows [2, 3]. These factors would directly determine urban airspace

availability and safety, both of which must be considered in operational planning.

Currently, a wide range of studies have focused on the evaluation and modeling of urban low-altitude airspace. Oh et al. [4] employed two indicators of airspace availability and population risk to identify feasible airspace and conduct connectivity testing using quadrant analysis and Pareto ranking. Yang et al. [5] systematically reviewed airspace design and risk assessment for urban air mobility (UAM), but the airspace design was not fully integrated with risk assessment as well as limited types of risk. Davies et al. [6] focused on the management of urban low-altitude airspace as well as the summarization of the feasibility analysis of unmanned aircraft system traffic management (UTM) systems. Doole et al. [7] proposed two urban airspace design concepts and compared safety, stability, and efficiency under different traffic demand densities. Xu et al. [8] reviewed the policies and some key technologies of UAV operations in low-altitude airspace but lacked of deep analysis of the UTM framework and practical guidance. Bae et al. [9] applied multiple ranking algorithms to evaluate airspace capacity across four delivery scenarios, but did not account for risk factors limiting its applicability. Lee et al. [10] analyzed the advantages and disadvantages of existing airspace allocation methods, yet the focus was more on task allocation than an in-depth study of airspace itself. Zhang et al. [11] constructed an airspace topology model based on ground population risk and airspace availability, but did not consider the spatiotemporal mobility of populations, and the low-resolution case maps restricted application value.

In addition to airspace availability evaluation and general ground-risk assessment, recent studies have also emphasized the influence of spatiotemporal population characteristics and uncertainty handling in dynamic environments. Oh and Yoon [12] conducted a data-driven risk analysis of unmanned aircraft system operations by incorporating the spatiotemporal characteristics of population distribution. Their study showed that high-resolution de facto population data can better reflect temporal variations in population exposure than residential population data, indicating the importance of dynamic population information in UAS population-risk assessment.

Uncertainty caused by unknown operating conditions has also been discussed in related engineering fields. For example, open-set classification methods [13] have been developed to identify unknown faults by using latent representation learning and time-frequency fusion, while domain generalization methods [14] have been used to improve fault diagnosis robustness under unknown operating conditions. In addition, recent studies on unsupervised image stitching have explored generative adversarial networks and feature frequency awareness algorithms [15], as well as attention mechanisms with deep homography estimation [16], to improve image alignment, visual feature representation, and spatial information reconstruction. These studies provide useful references for high-resolution urban spatial data acquisition and visual scene reconstruction, which are important for building accurate urban airspace evaluation datasets. Although these studies are not directly focused on urban low-altitude airspace evaluation, they provide useful methodological insights for handling temporal variations, unknown conditions, and uncertainty in dynamic systems.

Compared with these studies, the present work focuses on urban low-altitude airspace evaluation for UAV operations by integrating airspace availability, static risk, and dynamic risk into a unified voxel-based framework. The proposed framework considers both geometric accessibility under building constraints and multiple operational risks, including data transmission risk, obstacle collision risk, crash-induced fatality risk, property damage risk, and time-varying population exposure. It further links multi-risk assessment with feasible airspace delineation and connectivity analysis.

Overall, existing studies on urban low-altitude airspace evaluation can be broadly divided into availability-oriented and risk-assessment-oriented approaches. Availability-oriented methods mainly focus on the geometric accessibility and connectivity of airspace under the influence of buildings and other static obstacles, whereas risk-assessment-oriented methods emphasize the safety consequences caused by UAV operations, such as collision, crash-induced fatalities, population exposure, and property damage. However, these two types of methods are often developed separately. Availability evaluation alone cannot fully reflect the operational risks imposed on ground people, vehicles, and urban assets, while risk assessment is not always directly coupled with airspace delineation and connectivity evaluation.

Although some recent studies have attempted to combine airspace availability with population risk, most of them still rely on single-risk or dual-indicator frameworks. In complex urban environments, the feasibility of low-altitude airspace is jointly affected by geometric obstruction, communication conditions, obstacle collision risk, crash-induced fatality risk, property damage, societal impact, and time-varying population exposure. Therefore, a comprehensive evaluation framework integrating airspace availability, static risk, and dynamic risk is necessary for more reliable urban low-altitude airspace evaluation.

The main contributions of this study are summarized as follows:

(1) A three-indicator comprehensive evaluation framework is proposed for urban low-altitude airspace. Different from existing single-indicator or dual-indicator methods, the proposed framework integrates airspace availability, static risk, and dynamic risk, thereby evaluating urban airspace from the perspectives of geometric accessibility, environmental operational risk, and time-varying ground exposure.

(2) A multi-risk coupling mechanism is established by separating UAV operational risks into static and dynamic components. The static risk model integrates data transmission risk, obstacle collision risk, indirect fatality risk, and property damage risk, while the dynamic risk model incorporates direct fatality risk and societal impact risk under different population distribution scenarios. This design allows multiple heterogeneous risk factors to be mapped into a unified voxel-based evaluation framework.

(3) A two-stage airspace delineation strategy is developed by combining quadrant analysis with an improved Pareto ranking method. The quadrant analysis is used to identify preliminary feasible airspace under the constraints of low static risk, low dynamic risk, and high airspace availability, while the improved Pareto ranking further prioritizes the candidate voxels to generate the final feasible airspace.

(4) A high-resolution 3D urban airspace case study is conducted using real geographic information system (GIS) data from Changqing District, Jinan City. The results demonstrate the spatiotemporal variation of feasible airspace and show that higher-altitude layers, especially between 28 m and 40 m, provide better connectivity for UAV operations.

The remainder of this paper is organized as follows. Section 2 describes problems in urban airspace evaluation. Section 3 establishes the evaluation indicators and introduces methods. Section 4 generates preliminary and final feasible airspace maps. Section 5 conducts connectivity tests under both risk-oriented and availability-oriented conditions. Section 6 concludes the paper.

2. Problem description

In urban low-altitude airspace, the dense buildings and dynamically changing ground traffic pose significant safety challenges for UAV operations [17]. To mitigate the urban risk, some geofencing and similar technologies are often applied in practice to regulate urban areas around critical infrastructures. Scientifically and reasonably defined airspace is essential to ensure the safe operations of UAVs.

Most existing studies construct airspace models based on a single indicator failing to capture all characteristics of urban airspace for UAV operations. A few studies introduced dual indicators representing a certain amount of progresses but still with limitations.

This study focuses on the urban airspace below 40 m and establishes a three-indicator system to accurately model urban low-altitude airspace. These indicators are airspace availability, static risk, and dynamic risk. Airspace availability is used to quantify the feasibility of UAVs' flights within some specific space considering available voxels in a k-cuboid covered area that is calculated through the shortest number of hops between voxels in unobstructed and obstructed airspace. Static risk consists of data transmission risk, obstacle collision risk, indirect fatality risk, and property damage risk. To reduce subjectivity in risk aggregation, the four components are weighted using the global entropy weight method according to their spatial distribution and information uncertainty. The equal-weight scheme is used only as a baseline for comparison. Dynamic risk is composed of direct fatality risk and societal impact risk, which are mainly caused by population mobility and ground gatherings. To reduce subjective weighting and maintain consistency with the static risk aggregation, the weights of direct fatality risk and societal impact risk are also calculated using the global entropy weight method according to their spatial distribution and information uncertainty, rather than being preset as fixed equal values.

To further improve accuracy of the three-indicator model, three-dimensional voxels are employed to discretize the urban airspace into many cuboids with a fixed length, width, and height constructing a structured model. Combining a quadrant analysis and an improved Pareto ranking, the aforementioned three indicators are comprehensively evaluated and prioritized.

3. Methodology

The framework of urban airspace evaluation is described in Figure 1, which consists of the following steps. First, the urban airspace is discretized into 10 layers and the distance between each layer is 4 m. In this way, the height h of a specified urban airspace would be 40 m. Each layer is further divided into square grids with a side length of 10 m serving as elementary units. Second, the data of urban buildings, ground population, ground vehicles, and ground shelter factors are mapped onto the square grids in each layer to calculate the indicators of airspace availability, static risk, and dynamic risk. Third, a quadrant analysis method is applied with a given threshold to preliminarily filter airspace with low static risk, low dynamic risk, and high airspace availability (LLH). Finally, an improved Pareto ranking method is used to globally rank the filtered results and the top 70% are selected to generate the final feasible airspace map. There are no specific unified standards for the parameters in this framework, whose values are only determined according to user requirements and the actual urban environment.

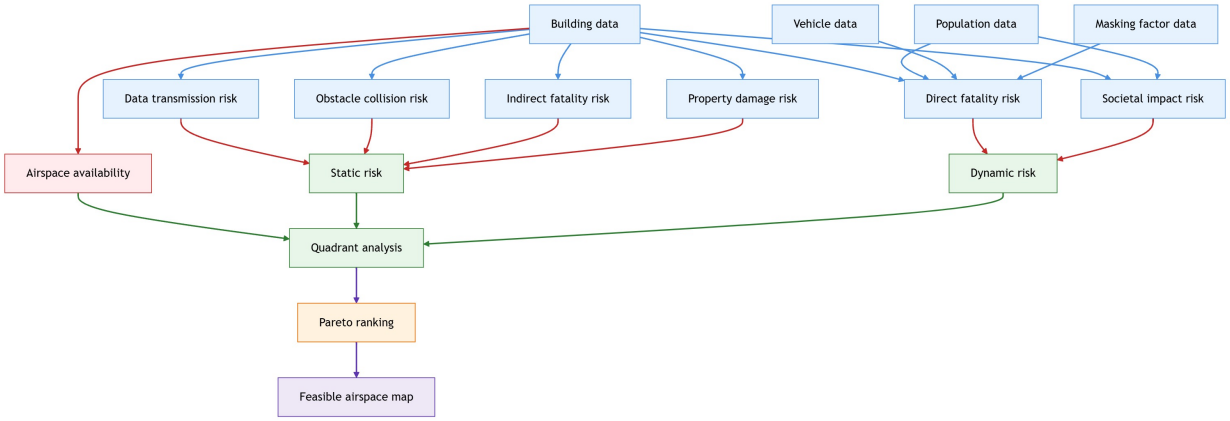

Figure 1. Framework of urban airspace evaluation.

Symbols and detailed definitions of key variables used in this paper are summarized in Table 1.

Table 1. Notation and definitions of key variables.

Symbol	Description	Unit/Range
$\alpha(i,k)$	Airspace availability of voxel i within the k-cuboid coverage range	$[0,1]$
k	Neighborhood parameter defining the local cuboid coverage range	Positive integer
$d_{\text{unobs}}(i,j)$	Minimum hop count from voxel i to voxel j in unobstructed airspace	–
$d_{\text{obs}}(i,j)$	Minimum hop count from voxel i to voxel j in obstructed airspace	–
R_{total}	Comprehensive static risk indicator	$[0,1]$
R_1–R_4	Data transmission risk, obstacle collision risk, indirect fatality risk, and property damage risk	$[0,1]$
l	Dynamic risk indicator	$[0,1]$
R_5 and R_6	Direct fatality risk and societal impact risk	$[0,1]$
h	UAV flight altitude or height layer	m
dist_{obs}	Distance between the UAV voxel and the nearest obstacle	m
w_1, w_2, w_3	Weight coefficients of static risk, dynamic risk, and airspace availability in Pareto ranking	$[0,1]$
Z	Objective value in the improved Pareto-ranking model	–

3.1. Construction of the airspace availability indicator

In urban low-altitude airspace, the ground buildings are treated as static obstacles with known positions representing key environmental constraints for safe UAVs' flights. During their flights, UAVs need to determine whether the voxels they are going through are occupied by static obstacles or not to assess their feasibilities [18]. The distribution map of ground buildings used in this paper is shown in Figure 2 including their accurate positions and heights.

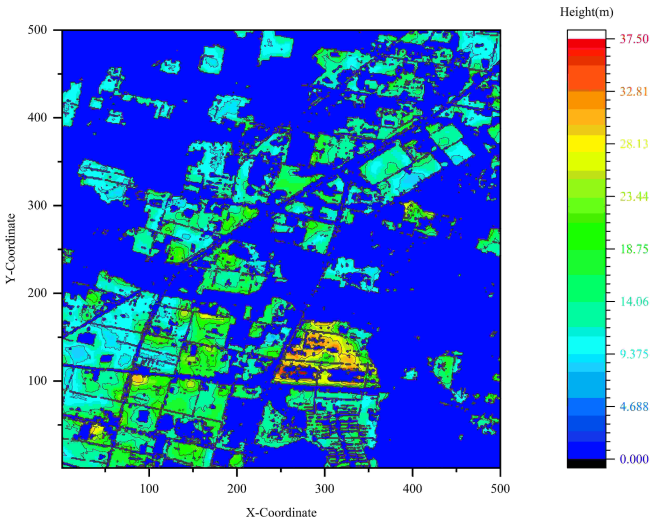

Figure 2. Distribution map of ground buildings.

To systematically evaluate the urban airspace availability, a voxel-based measurement method is developed in this paper by assessing voxel i within a k-cuboid covered area. Specifically, $d_{unobs}(i, j)$ is defined as a minimum hop count from a voxel i to a voxel j in an ideal unobstructed airspace, which is shown in Figure 3. This value reflects the shortest path length from a voxel i to a target voxel j when no obstacles are present.

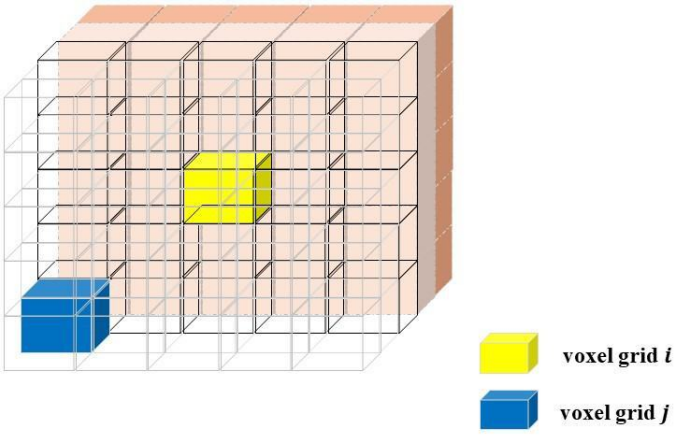

Figure 3. Unobstructed urban airspace.

Similarly, $d_{obs}(i, j)$ is defined as an actual minimum hop count from a voxel i to a voxel j in an obstructed airspace with static obstacles existing such as buildings. As a result, detours must happen by going through other unobstructed voxels as illustrated in Figure 4. Generally, $d_{obs}(i, j) \geq d_{unobs}(i, j)$. The difference between $d_{obs}(i, j)$ and $d_{unobs}(i, j)$ reflects the extent to which static obstacles affect the airspace capability, namely, the degree to which UAVs' flight paths are extended due to obstacle avoidance.

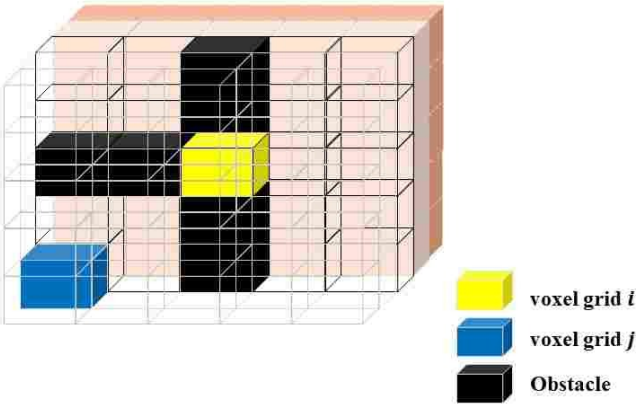

Figure 4. Obstructed urban airspace.

Corresponding to the construction of a k-cuboid area with a dimension of $5 \times 5 \times 5$, the parameter k is set as $k = 2$ in the model. In this way, there would be 125 voxels in a cuboid, whose size is $10\,\text{m} \times 10\,\text{m} \times 4\,\text{m}$. The voxel i is located at the center of a $5 \times 5 \times 5$ cuboid. Since $k = 2$ and the diagonal voxels are not considered, the minimum hop counts from a voxel i to other voxels in the six directions (up, down, left, right, front, and back) are all less than or equal to 2. The airspace coverage ratio is expressed as shown in Eq (3.1) [4]. $Airspace\_coverage(i, j)$ denotes an airspace coverage ratio from a voxel i to a voxel j.

$$Airspace\_coverage(i, j) = \begin{cases} \dfrac{d_{unobs}(i, j)}{d_{obs}(i, j)}, & \text{if} \quad \exists\, d_{obs}(i, j), \\ 0, & \text{otherwise.} \end{cases} \tag{3.1}$$

Based on the analysis, the airspace availability indicator $\alpha(i, k)$ of a voxel grid i within the k-cell coverage range is defined in Eq (3.2) [4], where S represents a set of voxels within the k-cuboid covered area.

$$\alpha(i, k) = \frac{1}{|S| - 1} \sum_{\substack{i \neq j \\ j \in S}} Airspace\_coverage(i, j). \tag{3.2}$$

3.2. Construction of the static risk indicator

The static risk indicator is composed of four categories of risk caused by UAV operations, which are data transmission risk, obstacle collision risk, indirect fatality risk, and property damage risk. All of these focus on the potential threats caused by some static obstacles, excluding dynamic factors such as pedestrians on the ground.

However, to improve the objectivity and flexibility of the risk assessment, the weights r_1, r_2, r_3, and r_4 can be dynamically adjusted using the global entropy weight method, which calculates the weights based on the spatial distribution and uncertainty of the risks. This adjustment eliminates subjectivity in assigning the weights and ensures the reproducibility of the comprehensive risk model.

The calculation of the global weight for the i-th risk is given by

$$r_i = \frac{d_i}{\sum_{k=1}^{4} d_k}, \quad \text{where} \quad d_i = 1 - e_i \quad \text{and} \quad e_i = -\frac{1}{\ln n} \sum_{j=1}^{n} p_{ij} \ln(p_{ij} + \epsilon). \tag{3.3}$$

Thus, the final comprehensive risk R_{total} is computed as

$$R_{\text{total}} = \sum_{i=1}^{4} r_i \cdot R_i. \tag{3.4}$$

Based on the global entropy weight method, the weights of data transmission risk, obstacle collision risk, indirect fatality risk, and property damage risk are calculated as 0.05477663, 0.40235398, 0.44517311, and 0.09769628, respectively, as shown in Table 2.

Table 2. Weights of static risk indicators calculated by the global entropy weight method.

Weight symbol	Risk component	Weight value
w_1	Data transmission risk	0.05477663
w_2	Obstacle collision risk	0.40235398
w_3	Indirect fatality risk	0.44517311
w_4	Property damage risk	0.09769628
Total	–	1.00000000

3.2.1. Data transmission risk

The stability of the continuous communication link between UAVs and operators is a core element to ensure safe execution of missions. Most current studies rely on simplified urban geometric models to simulate radio frequency propagation to handle complex reflections and diffraction phenomena, which thereby estimate the communication coverage of UAVs. This paper focuses on assessing the data transmission risk caused by communication link failures.

To achieve a spatial modeling of data transmission risk, the target airspace is discretized into 3D voxels. When a UAV is operating in a voxel, the data transmission risk is evaluated by determining the line-of-sight (LOS) status with its operator. When LOS exists, the data transmission risk value R_1 is 0. Vice versa, the data transmission risk value R_1 is 1, which is given in Eq (3.5) [19].

$$R_1 = \begin{cases} 0, & \text{if } \exists\, LOS, \\ 1, & \text{if } \nexists\, LOS. \end{cases} \tag{3.5}$$

3.2.2. Obstacle collision risk

The urban airspace is divided into 3D voxels which can be further represented as a form of a 3D matrix [20]. The distance between a UAV and urban obstacles is denoted with a variable $dist\_obs$, which is highly related to the obstacle collision risk [21]. When a UAV is approaching an obstacle, the value of $dist\_obs$ decreases and the obstacle collision risk increases significantly. Conversely, as the distance increases, the obstacle collision risk decreases gradually.

As the distance increases, to prevent the value of the obstacle collision risk from approaching zero indefinitely, a threshold Z_{min} is introduced. When $dist\_obs > Z_{min}$, it means that there is no collision risk between the UAVs and urban obstacles, whose corresponding obstacle risk value is set as 0. All voxels containing obstacles are regarded as no-fly zones and their corresponding collision risk is set to 1 with $dist\_obs = 0$. In addition, the performance of a UAV's navigation system is taken into account,

which is represented by defining an extra adjustment coefficient k_{GNSS}. The obstacle collision risk model can be expressed as Eq (3.6) [19]. R_2 is the value of the obstacle collision risk.

$$R_2 = \begin{cases} 1, & \text{if } dist\_obs = 0, \\ e^{-k_{GNSS} \cdot \frac{dist\_obs}{Z_{\min}}}, & \text{if } 0 \le dist\_obs \le Z_{\min}, \\ 0, & \text{if } dist\_obs > Z_{\min}. \end{cases} \tag{3.6}$$

To address this adjustment coefficient k_{GNSS}, a geometric dilution of precision (GDOP)-based method is introduced [22]. This GDOP method constructs a linear model matrix using positions of 20 satellites and the GDOP factor is then derived through the inversion of a covariance matrix. It is supposed that positions of a satellite i ($i = 1, 2, \ldots, 20$) and a receiver can be represented as (x_i, y_i, z_i) and (x_r, y_r, z_r), respectively. Based on the relative positions between them, a direction cosine matrix B is formulated as given in Eq (3.7). d_i ($i = 1, 2, \ldots, 20$) denotes the Euclidean distance between a receiver and a satellite i. The term -1 in matrix B represents a receiver clock bias in satellite signal propagation referring to the time offset between a receiver clock and a satellite clock.

$$B = \begin{bmatrix} \frac{x_1 - x_r}{d_1} & \frac{y_1 - y_r}{d_1} & \frac{z_1 - z_r}{d_1} & -1 \\ \frac{x_2 - x_r}{d_2} & \frac{y_2 - y_r}{d_2} & \frac{z_2 - z_r}{d_2} & -1 \\ \vdots & \vdots & \vdots & \vdots \\ \frac{x_{20} - x_r}{d_{20}} & \frac{y_{20} - y_r}{d_{20}} & \frac{z_{20} - z_r}{d_{20}} & -1 \end{bmatrix}. \tag{3.7}$$

The covariance matrix is given in Eq (3.8), which is denoted as Y. In this equation, B^T is a transpose of a direction cosine matrix in Eq (3.7).

$$Y = (B^T \cdot B)^{-1}. \tag{3.8}$$

The GDOP factor F_{GDOP} can be calculated by extracting diagonal elements of a covariance matrix Y with Eq (3.9). $Y[1, 1]$ is an estimated variance of a receiver's x-coordinate x_r. A smaller value of $Y[1, 1]$ indicates a more accurate estimation. Similarly, $Y[2, 2]$ is an estimated variance of a receiver's y-coordinate y_r. The smaller its value, the higher the estimation accuracy. $Y[3, 3]$ denotes an estimated variance of a receiver's z-coordinate z_r. Smaller values would indicate more accurate estimations. $Y[4, 4]$ represents an estimated variance of a receiver clock bias b, which reflects how the accuracy of time synchronization affects positioning precision.

$$F_{GDOP} = Y_{[1,1]} + Y_{[2,2]} + Y_{[3,3]} + Y_{[4,4]}. \tag{3.9}$$

Once the GDOP factor F_{GDOP} is obtained, the adjustment coefficient k_{GNSS} can be calculated using Eq (3.10). In this equation, $F_{GDOP}^{\max}$ is the maximum GDOP factor, which is set to 6. $F_{GDOP}^{\min}$ is the minimum GDOP factor, which that is set to 1. From Eq (3.10), it can be observed that $k_{GNSS} \in [0, 1]$.

$$k_{GNSS} = 1 - \frac{F_{GDOP}^{i} - F_{GDOP}^{\min}}{F_{GDOP}^{\max} - F_{GDOP}^{\min}}. \tag{3.10}$$

3.2.3. Indirect fatality risk

Indirect fatality risk refers to the potential harm to ground pedestrians when a UAV crashes after colliding with buildings in urban airspace [23]. To accurately quantify this risk, the urban building density is integrated with the probability distributions of UAVs' flight altitudes as shown in Eq (3.11). In this equation, P_{UCO} is a probability of a UAV colliding with buildings, N_{b_impact} denotes the number of buildings affected by a UAV's descent, and N_D^P represents the average number of fatalities with a value of 0.7537 [24].

$$R_3 = P_{UCO} \cdot N_{b\_impact} \cdot N_D^P. \tag{3.11}$$

To calculate P_{UCO}, it is assumed that UAV flight altitude follows a normal distribution as shown in Eq (3.12) [25]. In this equation, H_{high} and H_{low} are the upper and lower bounds determined by building heights in urban areas. Also, μ and σ represent the mean and standard deviation of a UAVs' flight altitude.

$$P_{UCO} = \int_{H_{low}}^{H_{high}} \frac{1}{\sqrt{2\pi}\,\sigma} \exp\left(-\frac{(h-\mu)^2}{2\sigma^2}\right) dh. \tag{3.12}$$

Furthermore, N_{b_impact} can be obtained with Eq (3.13). σ_b is the building density and S_{b_hit} is an estimated ground area affected by a crashed UAV.

$$N_{b\_impact} = \sigma_b \cdot S_{b\_hit}. \tag{3.13}$$

Equation (3.14) shows how to calculate the affected ground area S_{b_hit}, in which r_{UAV} denotes the radius of a crashed UAV.

$$S_{b\_hit} = \pi \cdot r_{UAV}^2. \tag{3.14}$$

3.2.4. Property damage risk

Property damage risk refers to the potential loss caused by UAV collisions with urban properties due to their system failures during flights. It is mainly determined by the impact kinetic energy of collisions and the loss coefficient.

In this paper, three collision scenarios are defined. The first is a collision with vegetation-dense areas such as green spaces and parks, which are classified as low risk with a low loss coefficient. The second is a collision with open areas such as roads and parking lots, which are classified as medium risk with a moderate loss coefficient. The third is a collision with buildings and critical infrastructures, which are classified as high risk with a high loss coefficient. The loss coefficients for these three scenarios are given in

$$g_{obs} = \begin{cases} 0.3, & \text{Collision Scenario 1,} \\ 0.7, & \text{Collision Scenario 2,} \\ 1, & \text{Collision Scenario 3.} \end{cases} \tag{3.15}$$

In Eq (3.15), g_{obs} is the defined loss coefficient with values of 0.3, 0.7, and 1, which is determined by collisions between UAVs and different types of ground objects [19]. By combining UAV's impact kinetic energy with the defined loss coefficients, a property damage risk model can be established as shown in Eq (3.16) [19].

$$R_4 = P_{crash} \cdot g_{obs} \cdot \frac{E_{impact}}{E_{\max}}. \tag{3.16}$$

The property damage risk is denoted as R_4. P_{crash} is the probability of a UAV's system failure. g_{obs} is the defined loss coefficient, which can be obtained using Eq (3.15). E_{impact} refers to the actual impact kinetic energy when UAVs collide with ground objects. E_{max} is the impact kinetic energy corresponding to the maximum velocity.

3.3. Population distribution estimation

In our previous research, K-means clustering and linear regression were employed to obtain the population density distributions combining with WorldPop data and the Seventh National Population Census data. Based on current existing population data, the analysis of static population distribution becomes the focus [18]. To simplify the modeling, it is assumed that there is no population mobility within the ground areas and the total population remains constant. Land use classification is needed as the basic dataset, which is aligned with the population density distribution. Land use classification results are presented in Table 3.

Table 3. Land-use classification.

Numbering	Land use classification
0	High cement buildings
1	Low buildings with red tile roofs
2	Low buildings with brown tile roofs
3	Low buildings with gray roofs
4	Low buildings with blue metal roofs
5	Low buildings with red metal roofs
6	Silver-gray industrial area
7	Blue-white industrial area
8	Blue industrial area
9	Cement ground
10	Grassland
11	Tall vegetation
12	Highway
13	Lake
14	Loess Land

It should be noted that the population distributions at 10:00 A.M. and 10:00 P.M. are designed as two representative scenarios rather than exact real-time population mobility patterns. The 10:00 A.M. scenario represents typical daytime working and outdoor activities, while the 10:00 P.M. scenario represents nighttime residential concentration. The purpose of introducing these two scenarios is to examine whether the proposed airspace evaluation framework can respond to temporal variations in ground population exposure.

Since fine-grained, real-time population mobility data, such as anonymized mobile phone signaling data or continuous pedestrian flow observations, are not available for the study area, land-use categories, WorldPop data, and census-based population information are used as alternative spatial constraints for estimating population redistribution. The assumption of a constant total population is adopted to ensure that the difference between the two scenarios is mainly caused by spatial

redistribution rather than changes in the total population scale.

Although this simplification cannot fully capture complex urban mobility patterns, it provides a controllable way to evaluate the influence of temporal population redistribution on dynamic risk and feasible airspace. Future work will incorporate mobile phone signaling data, traffic flow observations, and multi-source urban sensing data to further improve the accuracy of dynamic population modeling.

According to the types given in Table 3, the distributions of land uses in a specified urban area are given in Figure 5. In this part, the spatial distributions of urban populations at 10:00 A.M. and 10:00 P.M. are estimated based on different land uses.

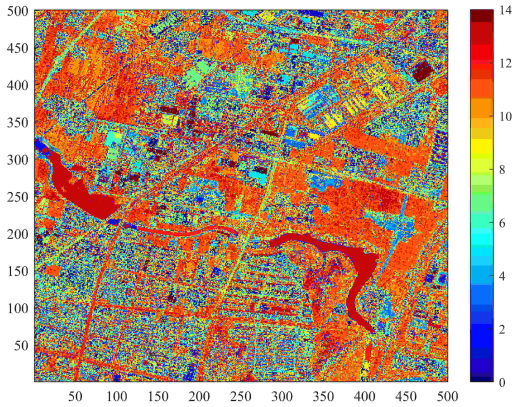

Figure 5. Distributions of different land uses.

At 10:00 A.M., normally, most people have arrived at their workplaces and only a small portion remain in residential areas. In this way, it is assumed that 80% of the population is distributed across industrial land and outdoor public spaces corresponding to the land-use categories numbered as 6, 7, 8, 9, 10, 12, 13, and 14. The remaining 20% would be assumed to be located in their residential areas, which corresponds to the categories numbered as 0, 1, 2, 3, 4, and 5. The population is distributed evenly for each land-use category. The population distributions at 10:00 A.M. of specified urban areas are shown in Figure 6.

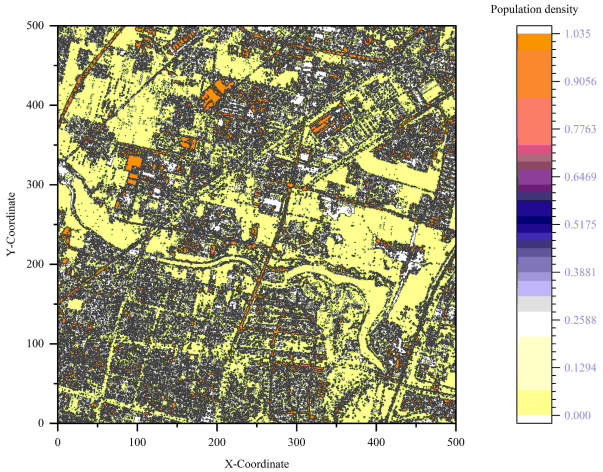

Figure 6. Population distributions at 10:00 A.M.

At 10:00 P.M., it is assumed that the entire population has returned to residential areas with no individuals remaining in industrial or other non-residential areas. Based on this assumption, 100% of the population is allocated in residential areas corresponding to categories numbered as 0, 1, 2, 3, 4, and 5. Also an even distribution strategy is applied across all the residential types. The population distributions at 10:00 P.M. are given in Figure 7.

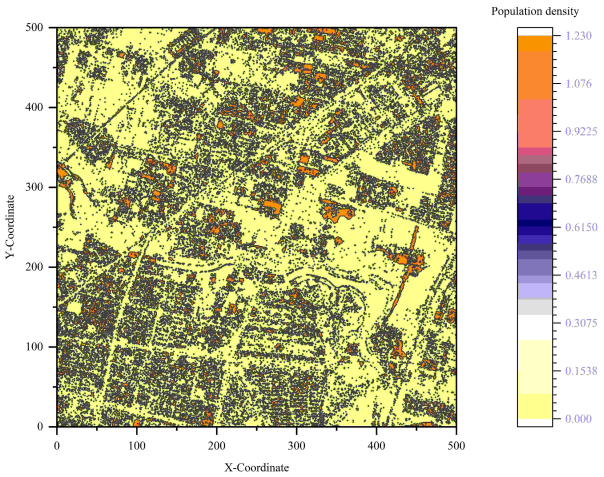

Figure 7. Population distributions at 10:00 P.M.

3.4. Construction of the dynamic risk indicator

Based on the estimations of the population distributions at 10:00 A.M. and 10:00 P.M., a dynamic risk indicator model is constructed, composed of the direct fatality risk R_5 and societal impact risk R_6, with weights dynamically calculated through the global entropy weight method. This dynamic risk indicator is defined to evaluate the impacts of UAV operations on ground people, as shown in Eq (3.17). R_5 is the direct fatality risk, and R_6 is the societal impact risk. The weights are dynamically adjusted based on the variability and uncertainty of each risk using the global entropy weight method. The specific calculation formula is as follows:

$$l = w_5 R_5 + w_6 R_6, \tag{3.17}$$

where w_5 and w_6 are the weights of the direct fatality risk and societal impact risk, respectively, calculated through the global entropy weight method, and they satisfy $w_5 + w_6 = 1$.

$$w_5 = \frac{1 - H_5}{\sum_{i=1}^{2}(1 - H_i)}, \quad w_6 = \frac{1 - H_6}{\sum_{i=1}^{2}(1 - H_i)}, \tag{3.18}$$

where H_5 and H_6 are the entropy values of the direct fatality risk and societal impact risk, respectively, reflecting the variability or uncertainty of each risk.

3.4.1. Direct fatality risk

Direct fatality risk refers to the risk of UAVs' failure during operations in urban airspace, which results in a crash that collides with pedestrians or vehicles on the ground causing fatalities. The direct

fatality risk R_5 can be obtained using Eq (3.19) including the risk to pedestrians $R_{\text{fat\_p}}$ and the risk to vehicles $R_{\text{fat\_v}}$ [19]. The two share the same weight coefficient.

$$R_5 = 0.5 \cdot R_{\text{fat\_p}} + 0.5 \cdot R_{\text{fat\_v}}. \tag{3.19}$$

Equation (3.20) presents a risk model of ground pedestrians that is defined as the number of fatalities per UAV flight hour [26]. In this equation, P_{crash} denotes the probability of a UAVs' failure, which depends on system reliability. N^p_{hit} is the number of pedestrians affected by the crashing UAV, which is related to ground population density. R^p_f is a fatality rate of pedestrians who are struck, which depends on a UAV's weight and the fallen height.

$$R_{\text{fat\_p}} = P_{\text{crash}} \cdot N^p_{\text{hit}} \cdot R^p_f. \tag{3.20}$$

To obtain an accurate value of N^p_{hit}, the population density and the location where UAVs crash are used as shown in Eq (3.21). In this equation, p_p represents the ground population density and S_{hit} denotes the affected ground areas.

$$N^p_{\text{hit}} = p_p \cdot S_{\text{hit}}. \tag{3.21}$$

When the fatality rate of ground individuals R^p_f is being derived, both the impact kinetic energy of UAVs and shielding effects of trees and buildings are considered. The kinetic energy could determine the severity of UAVs' impact, while shielding effects would mitigate the fatal consequences for pedestrians and vehicles. R^p_f is calculated using Eq (3.22). M_f is a shielding coefficient that can be obtained from field measurements with $M_f \in (0, 1]$. E_{impact} denotes the impact kinetic energy of crashed UAVs [27]. When $M_f = 0.5$, it corresponds to the impact energy leading to a fatality rate of 50%. When a shielding coefficient M_f approaches 0, it corresponds to an energy threshold required to cause fatalities. In this paper, $\alpha = 10^6$ J and $\beta = 100$ J are adopted.

$$R^p_f = \frac{1}{1 + \sqrt{\frac{\alpha}{\beta}} \left(\frac{\beta}{E_{\text{impact}}} \right)^{\frac{1}{4M_f}}}. \tag{3.22}$$

To calculate the impact energy E_{impact} of a crashed UAV, its impact velocity must be obtained first. During the descent, a UAV is affected by a vertical drag force, which is expressed by Eq (3.23). This depends on size, material, and air density. F_d is a vertical drag force. R_l is a drag coefficient related to the UAV's model. ρ_{air} is the air density (1.225 kg/m^3 at sea level) and v_T is the true falling velocity.

$$F_d = \frac{1}{2} \cdot R_l \cdot S_{\text{hit}} \cdot \rho_{\text{air}} \cdot v^2_T. \tag{3.23}$$

Accordingly, the acceleration a of a falling UAV can be calculated with Eq (3.24) [28]. F_g is the gravitational force ($F_g = mg$, $g = 9.8$ m/s^2). By using this acceleration a, Eq (3.24) gives the UAV's ground-impact velocity at time t.

$$a = \frac{F_g - F_d}{m} = g - \frac{R_l \cdot S_{\text{hit}} \cdot \rho_{\text{air}} \cdot v^2_T}{2m}. \tag{3.24}$$

In Eq (3.25), v is the impact velocity and t denotes the time elapsed from a failure event to a ground impact. h represents the UAV's height above the ground at the moment of failure [27].

$$v = \int_0^t \left(g - \frac{R_l \cdot S_{\text{hit}} \cdot \rho_{\text{air}} \cdot v_T^2}{2m} \right) dt = \sqrt{\frac{2mg}{R_l \cdot S_{\text{hit}} \cdot \rho_{\text{air}}} \left(1 - e^{-\frac{h \cdot R_l \cdot S_{\text{hit}} \cdot \rho_{\text{air}}}{m}} \right)}. \tag{3.25}$$

Finally, the kinetic energy E_{impact} of a crashed UAV can be calculated using Eq (3.26), in which m is the UAV mass and v is the impact velocity obtained with Eq (3.25). Given the kinetic energy E_{impact}, the fatality rate R_f^p is then calculated according to Eq (3.22).

$$E_{\text{impact}} = \tfrac{1}{2} \cdot m \cdot v^2. \tag{3.26}$$

Similarly, based on the above analysis, the risk imposed to ground vehicles, denoted as $R_{\text{fat\_v}}$, can be defined as the number of fatalities per the UAV's flight hour, which is shown in Eq (3.27). N_{hit}^v represents the number of vehicles impacted by fallen UAVs, which is related to the vehicle density and affected ground areas [29]. R_f^v is an average fatality rate in such accidents and can be calculated as (total number of traffic accident fatalities per year) / (total number of traffic accidents per year).

$$R_{\text{fat\_v}} = P_{\text{crash}} \cdot N_{\text{hit}}^v \cdot R_f^v. \tag{3.27}$$

Equation (3.28) calculates the number of vehicles that are struck by a crashed UAV, where S_{hit} is the affected ground area and p_v denotes the vehicle density of the road network.

$$N_{\text{hit}}^v = S_{\text{hit}} \cdot p_v. \tag{3.28}$$

3.4.2. Societal impact risk

Societal impact risk refers to the noise disturbances and negative effects of UAVs that are imposed on pedestrians on the ground. It occurs only when pedestrians are within the effective propagation range of UAVs' noise (distance ≤ 30 m), while unpopulated areas are not affected. Assuming a UAV operates in a grid i, its societal impact risk R_6 is calculated based on ground population density and distance considering 24 surrounding neighboring grids ($j = 1, 2, \ldots, 24$), which is shown in Eq (3.29) [26]. In this equation, L_h is a reference noise whose value is 70 dB [30]. ω is a conversion coefficient from noise intensity to noise level and h is a UAV's flight altitude. d_{noise} denotes a horizontal distance between the center of a UAV's operating grid and the center of the most affected neighboring grid.

$$R_6 = L_h \cdot \omega \cdot \frac{1}{d_{\text{noise}}^2 + h^2}. \tag{3.29}$$

To determine a neighboring grid j that has the greatest impact on grid i, Eq (3.30) calculates its weighted value S_C^j, where p_j represents the population density and d_{ij} is the horizontal distance from grid i. The grid with the maximum S_C^j is selected; at this point, the horizontal distance between grid i and the selected grid j is taken as the d_{noise} of grid i, and its population density and distance to grid j are then used as the key parameters for calculating the societal impact risk.

$$S_C^j = p_j \times \frac{1}{d_{ij}}, \quad j = 1, 2, \ldots, 24. \tag{3.30}$$

3.5. Quadrant analysis

The objective of airspace management is to scientifically design an urban airspace structure at a strategic level to ensure both safe and efficient uses of resources. In this part, a method of quadrant analysis is applied to classify airspace units and determine their feasibilities based on a given criteria.

Three indicators of dynamic risk, static risk, and airspace availability are analyzed at 10:00 A.M. and 10:00 P.M. Each continuous indicator is divided into high and low according to predefined thresholds. Accordingly, all the airspace units are classified into eight categories, which are LLL, LLH, LHL, HLL, HHL, HLH, HHH, and LHH. These classifications are then converted into a preliminary feasible airspace map, where the LLH category (low dynamic risk, low static risk, and high airspace availability) is identified as the preferred airspace.

3.6. Pareto ranking

Based on the results of a quadrant analysis, a mechanism of Pareto ranking is incorporated to identify non-dominated solutions among multiple conflicting indicators. The traditional Pareto ranking requires pairwise comparisons of each voxel with all the others, resulting in a high computational complexity, which is unsuitable for the high-resolution 3D airspace of 2.5 million voxels in this paper.

To address this problem, an alternative method based on an objective function is proposed. As given in Eq (3.31), the static risk, dynamic risk, and urban airspace availability are considered to score and rank each voxel of a specified urban airspace. The top 70% are selected as a solution set, achieving the multi-objective trade-offs while reducing computational burden significantly. In this way, it would be suitable for rapid screening and authorization decisions in large-scale 3D airspace.

$$Z = w_1 \frac{f_{i,h} - f_{\min}}{f_{\text{threshold}} - f_{\min}} + w_2 \frac{l_{i,h} - l_{\min}}{l_{\text{threshold}} - l_{\min}} - w_3 \frac{\alpha_{i,h} - \alpha_{\text{threshold}}}{\alpha_{\max} - \alpha_{\text{threshold}}}. \tag{3.31}$$

Here, w_1, w_2, and w_3 are three weight coefficients with $0 \le w_i \le 1$ $(i = 1, 2, 3)$ and $w_1 + w_2 + w_3 = 1$. $f_{i,h}$ denotes the static risk at location i and height h. $f_{\min}$ is the minimum value of the static risk and $f_{\text{threshold}}$ is a threshold for the static risk. $l_{i,h}$ represents the dynamic risk at location i and height h. $l_{\min}$ and $l_{\text{threshold}}$ are the minimum value and threshold for dynamic risk, respectively. $\alpha_{i,h}$ is the airspace availability at location i and height h. Similarly, $\alpha_{\max}$ and $\alpha_{\text{threshold}}$ are the maximum value and threshold for airspace availability,respectively.

4. Validations and a case study

To validate the methodology proposed in this paper, an urban area of 5 km × 5 km in Changqing District, Jinan City, Shandong Province, is selected as a case study, as shown in Figure 8. Various ground features are included in this selected urban region, such as residential areas, schools, public facilities, and infrastructures.

A UAV manufactured by Da-Jiang Innovations (DJI) with a model of M210-RTK is used to assess its caused ground risk, after which an urban risk map is generated and airspace connectivity is validated.

Figure 8. Case study map of Changqing District, Jinan City.

The specifications of DJI M210-RTK are shown in Table 4, with a mass of 4.27 kg, a length of 0.887 m, and a width of 0.880 m. The frontal area is 0.234 m^2 and the probability of in-flight failure is set to 3.42×10^{-4}.

Table 4. Parameters of DJI M210-RTK UAV.

Parameter	Value
Mass	4.27 kg
Length	0.887 m
Width	0.880 m
Frontal area	0.234 m^2
P_{crash}	3.42×10^{-4}

4.1. Assessment of airspace availability

To assess the urban airspace availability in Figure 8, a voxel-based method is used to evaluate voxels at location i within a covered k-cuboid area, where $k = 2$. The resulting availability map up to a height of 40 m is shown in Figure 9, consisting of 10 layers at 4 m intervals.

As shown in Figure 9, the urban airspace availability around $(50, 500)$ and $(500, 0)$ in Layer 1 is close to 1, indicating favorable conditions for UAV operations. By contrast, the availability around $(0, 0)$ is close to 0 due to dense building obstructions.

As altitude increases, the airspace availability at $(0, 0)$ gradually reaches 1 in Layer 10, indicating fully unobstructed airspace. In general, urban airspace availability expands with altitude, improving accessibility. However, the availability at $(300, 150)$ in Layer 10 remains slightly below 1, implying that nearby buildings at 40 m still affect the high-altitude passage.

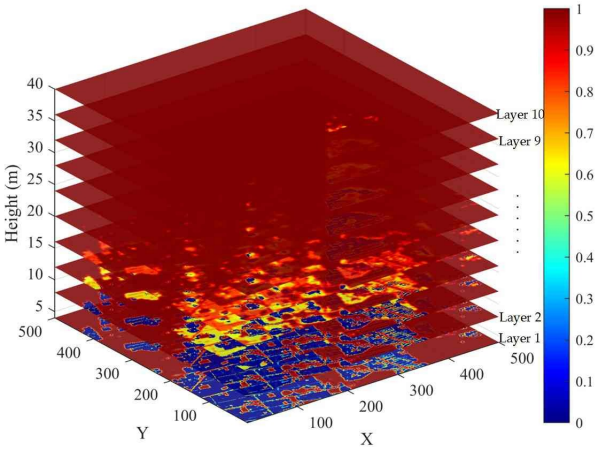

Figure 9. 3D airspace availability map.

For clarity, Layer 1, Layer 4, Layer 7, and Layer 10 are selected to show the distribution of urban airspace availability in Figure 10.

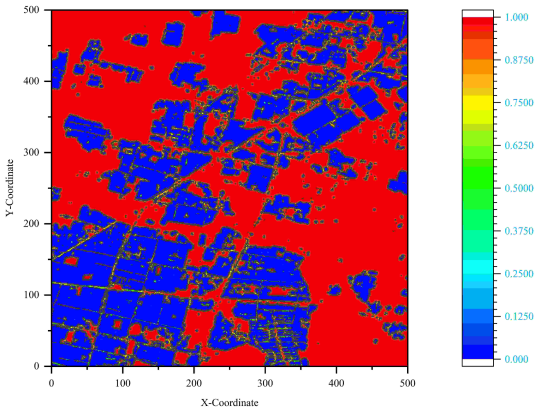

(a) First layer with a height of 4 m

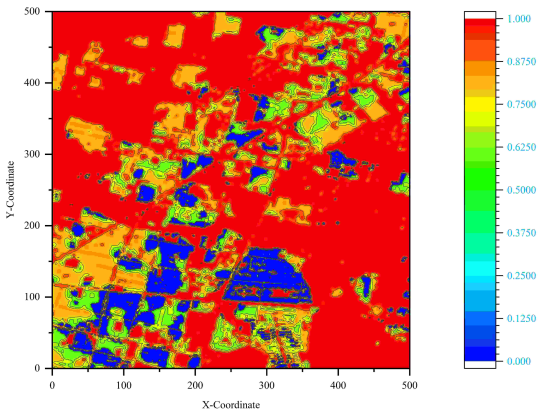

(b) Fourth layer with a height of 16 m

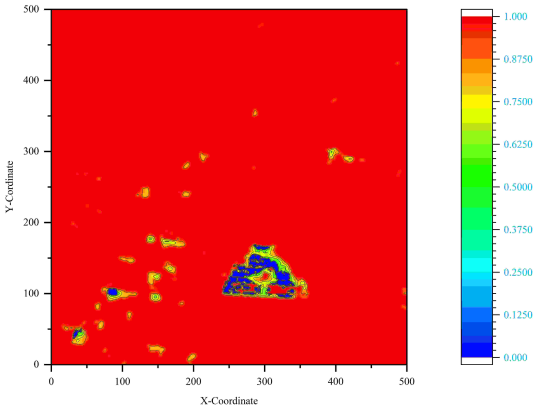

(c) Seventh layer with a height of 28 m

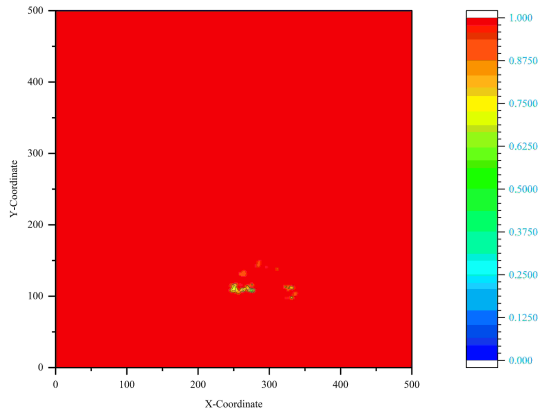

(d) Tenth layer with a height of 40 m

Figure 10. Four layers of urban airspace availability.

As shown in Figure 10, urban airspace availability increases with altitude. In Layer 1, the availability is zero around $(0, 0)$, $(320, 150)$, $(150, 275)$, and $(500, 500)$, indicating dense building clusters and obstructed airspace. With increasing altitude, availability improves in most areas except near $(320, 150)$. In Layer 7, only a few voxels remain unavailable, while most approach 1. Because the tallest buildings in the study area, about 37 m high, are located near $(320, 150)$, partial obstruction still remains in Layer 10, whereas most other high-altitude airspace is nearly unobstructed.

4.2. Sensitivity analysis of key parameters

To improve the reproducibility and robustness of the proposed method, a sensitivity analysis was conducted for the key parameters that may affect the urban airspace evaluation results. The analyzed parameters include the value of k in the k-cuboid coverage range, as shown in Table 5; the thresholds of airspace availability, static risk, and dynamic risk in the quadrant analysis, as shown in Table 6; and the weight coefficients of static risk, dynamic risk, and airspace availability in the improved Pareto ranking method, as shown in Table 7.

The value of k determines the spatial coverage range used to calculate the local airspace availability of each voxel. To examine the influence of k on the airspace availability evaluation, four values of k, namely, $k = 1$, $k = 2$, $k = 3$, and $k = 4$, were tested. The mean airspace availability was used as the evaluation criterion. A larger mean airspace availability indicates better overall airspace accessibility and weaker obstruction effects caused by buildings.

As shown in Table 5, the case of $k = 2$ achieves the highest mean airspace availability among the tested settings. Compared with $k = 1$, the $5 \times 5 \times 5$ cuboid coverage range can better capture the influence of surrounding obstacles on local airspace accessibility. Compared with $k = 3$ and $k = 4$, $k = 2$ avoids introducing excessive distant voxel information and maintains a moderate computational scale. Therefore, $k = 2$ is selected in this study for the construction of the airspace availability indicator.

Table 5. Sensitivity analysis of the value of k for airspace availability evaluation.

Scenario	Value of k	Cuboid size	Number of voxels	Mean airspace availability
k1	1	$3 \times 3 \times 3$	27	0.869167
k2	2	$5 \times 5 \times 5$	125	0.875084
k3	3	$7 \times 7 \times 7$	343	0.867384
k4	4	$9 \times 9 \times 9$	729	0.861028

For the quadrant analysis, the thresholds of airspace availability, static risk, and dynamic risk directly determine the preliminary feasible airspace. To select suitable threshold combinations for the 10:00 A.M. and 10:00 P.M. scenarios, the overall proportion of feasible airspace was used as the evaluation criterion. A larger feasible airspace proportion indicates that more voxels satisfy the constraints of high airspace availability, low static risk, and low dynamic risk under the corresponding threshold combination.

As shown in Table 6, the feasible airspace proportion varies under different threshold combinations. For the 10:00 A.M. scenario, Threshold 9 achieves the largest feasible airspace proportion of 0.68829. Although Threshold 5 also obtains a relatively high value of 0.68761, it is still slightly lower than that of Threshold 9. For the 10:00 P.M. scenario, Threshold 9 also achieves the largest feasible airspace proportion of 0.69988, which is slightly higher than Threshold 7 with a value of 0.69974. These results

indicate that Threshold 9 provides the best overall feasible airspace proportion under both the morning and evening scenarios.

Table 6. Sensitivity analysis of quadrant-analysis thresholds at 10:00 A.M. and 10:00 P.M.

Threshold	Airspace availability	Static risk	Dynamic risk	10:00 A.M.	10:00 P.M.
Threshold 1	0.50	0.40	0.40	0.46761	0.46961
Threshold 2	0.75	0.45	0.45	0.54067	0.53961
Threshold 3	0.80	0.50	0.50	0.61874	0.62483
Threshold 4	0.85	0.55	0.55	0.68489	0.69415
Threshold 5	0.90	0.60	0.60	0.68761	0.69209
Threshold 6	0.95	0.65	0.65	0.67372	0.67778
Threshold 7	1.00	0.70	0.70	0.686	0.69974
Threshold 8	0.72	0.42	0.44	0.51965	0.52063
Threshold 9	**0.90**	**0.55**	**0.53**	**0.68829**	**0.69988**
Threshold 10	0.82	0.52	0.53	0.68303	0.69385

Therefore, the thresholds of airspace availability, static risk, and dynamic risk are set to 0.90, 0.55, and 0.53, respectively, for the subsequent quadrant analysis. This threshold combination can retain a relatively large feasible airspace while maintaining constraints on static and dynamic risks.

After the preliminary feasible airspace was obtained through quadrant analysis, the improved Pareto ranking method was further applied to rank the candidate voxels. Since the same top 70% selection ratio was adopted for all parameter combinations, the number of final selected voxels mainly depends on the size of the preliminary feasible airspace. Therefore, the feasible airspace proportion is not suitable as the only criterion for evaluating the sensitivity of the improved Pareto ranking parameters.

To examine the influence of airspace availability, static risk, and dynamic risk parameters on the ranking results, the mean ranking score of the selected voxels was used as the evaluation criterion. A smaller mean ranking score indicates that the selected voxels have lower static risk, lower dynamic risk, and higher airspace availability under the corresponding parameter combination.

As shown in Table 7, different parameter combinations have only a slight influence on the mean ranking score, but certain differences can still be observed. A smaller mean ranking score indicates that the selected voxels have lower static risk, lower dynamic risk, and higher airspace availability. For the 10:00 A.M. scenario, Combination 5 achieves the lowest mean ranking score of 0.13323, indicating the best overall ranking performance in the morning scenario. For the 10:00 P.M. scenario, several parameter combinations show the same mean ranking score of 0.12657 in the table. This is because the values are rounded to five decimal places, and the minor differences among these combinations may occur in higher decimal places. Therefore, these very small numerical differences are not further discussed in detail.

Table 7. Sensitivity analysis of indicator parameter combinations in the improved Pareto ranking method.

Combination	Airspace availability	Static risk	Dynamic risk	Mean ranking score	
				10:00 A.M.	10:00 P.M.
Combination 1	0.15	0.60	0.60	0.13335	0.12657
Combination 2	0.20	0.65	0.65	0.13328	0.12657
Combination 3	0.25	0.70	0.70	0.13325	0.12657
Combination 4	0.25	0.75	0.75	0.13324	0.12657
Combination 5	**0.25**	**0.80**	**0.80**	**0.13323**	**0.12657**
Combination 6	0.30	0.80	0.80	0.13325	0.12657
Combination 7	0.35	0.80	0.80	0.13327	0.12657
Combination 8	0.25	0.85	0.80	0.13325	0.12658
Combination 9	0.25	0.80	0.85	0.13329	0.12663
Combination 10	0.30	0.85	0.85	0.13327	0.12657

Overall, Combination 5 achieves the lowest mean ranking score at 10:00 A.M. and remains among the lowest-ranking-score combinations at 10:00 P.M., demonstrating good stability and applicability under different time scenarios. Therefore, Combination 5 is selected for the subsequent improved Pareto ranking analysis. The airspace availability parameter, static risk parameter, and dynamic risk parameter are set to 0.25, 0.80, and 0.80, respectively.

4.3. Results of quadrant analysis

By integrating the indicators of airspace availability, static risk, and dynamic risk at two typical time points (morning and evening), a multi-dimensional quadrant analysis is performed to preliminarily identify the feasible urban airspace from 0 m to 40 m. Based on the sensitivity analysis, the threshold results shown in Table 8 were obtained. Under these thresholds, the proportion of feasible airspace is improved compared to the maximum value among the other nine scenarios.

Table 8. Thresholds for quadrant analysis.

Parameter	Value
Airspace availability	0.9
Static risk	0.55
Dynamic risk	0.53

A voxel is identified as preliminary feasible airspace only when airspace availability ≥ 0.9, static risk ≤ 0.55, and dynamic risk ≤ 0.53. Based on these criteria, the 3D preliminary feasible airspace from 0 m to 40 m at 10 A.M. is generated, as shown in Figure 11. The feasible airspace is limited from Layer 1 to Layer 5, increases gradually from Layer 6, and becomes fully feasible in Layer 10. This is because lower layers are constrained by lower availability and higher static and dynamic risks, while the wider ground population distribution at 10 A.M. further compresses the feasible airspace near the ground.

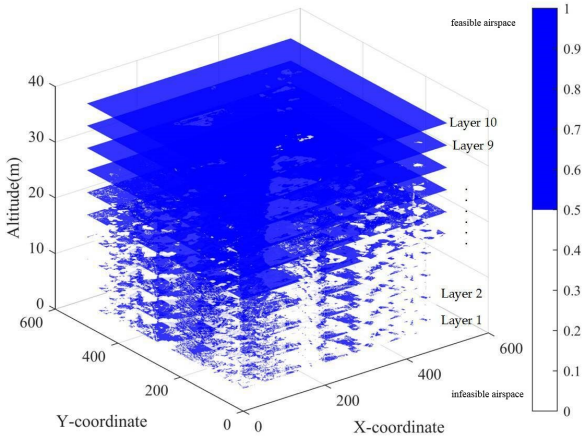

Figure 11. 3D preliminary feasible airspace at 10 A.M.

Four representative layers are extracted, which are Layer 1, Layer 4, Layer 7, and Layer 10. Four layers of preliminary feasible airspace at 10 A.M. are shown in Figure 12. In Layer 1, the proportion of preliminary feasible airspace is extremely low with only some scattered areas around $(75, 275)$ and $(450, 275)$. As the altitude increases, the scope of preliminary feasible airspace expands greatly. Especially in Layer 4, some larger areas around $(50, 50)$ and $(450, 275)$ become feasible. In Layer 7, the feasible airspace becomes dominant, except for a small area near $(200, 175)$. Similarly, only few infeasible areas remain around $(250, 125)$ in Layer 10, while most voxels are identified as feasible.

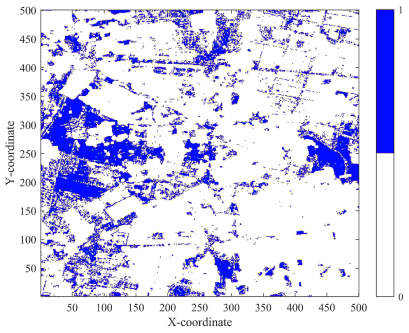

(a) First layer with a height of 4 m

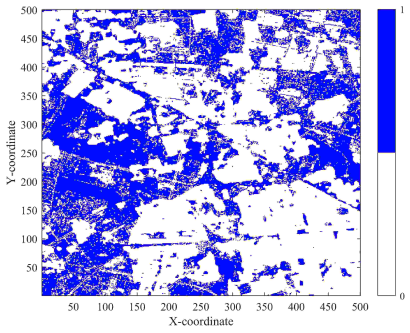

(b) Fourth layer with a height of 16 m

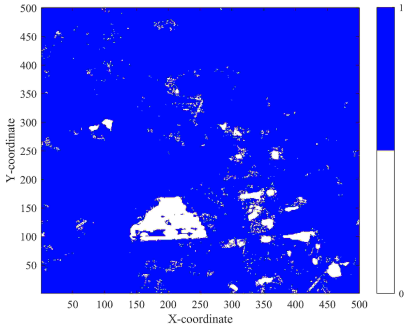

(c) Seventh layer with a height of 28 m

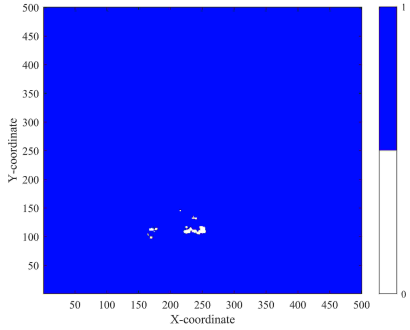

(d) Tenth layer with a height of 40 m

Figure 12. Four layers of preliminary feasible airspace at 10 A.M.

A quadrant analysis is conducted for the feasible airspace from 0 m to 40 m at 10:00 P.M. to identify preliminary feasible airspace. The thresholds are used as given in Table 6 requiring each voxel to satisfy its airspace availability ≥ 0.9, static risk ≤ 0.55, and dynamic risk ≤ 0.53 simultaneously. The 3D distribution of preliminary feasible airspace is generated as shown in Figure 13. It shows that from Layer 1 to Layer 5, the preliminary feasible airspace is relatively small. Starting at Layer 6, it increases significantly, and in Layer 10, it almost covers the entire airspace. This trend is consistent with the results at 10:00 A.M. indicating that higher altitude would improve the feasibility of urban airspace.

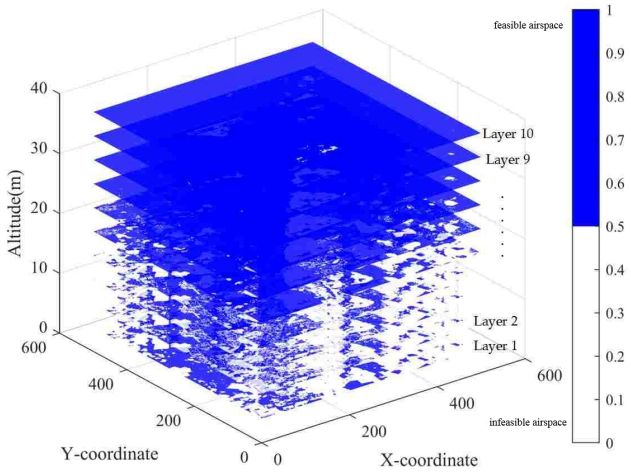

Figure 13. 3D preliminary feasible airspace at 10 P.M.

Further, Layer 1, Layer 4, Layer 7, and Layer 10 are all extracted to compare the feasibilities of urban airspace, which are given in Figure 14. In Layer 1, the preliminary feasible airspace is only distributed near the locations of $(50, 250)$ and $(450, 250)$ sporadically. In Layer 4, some feasible airspace appears around $(50, 50)$, although infeasible airspace remains large. The feasible airspace in Layer 7 expands significantly with only few infeasible zones near $(200, 150)$ and $(430, 100)$. In Layer 10, the feasible airspace almost covers the entire layer except the regions near $(250, 120)$. Compared with 10:00 A.M., the feasible airspace of Layer 1 is larger at 10:00 P.M. It is because the population is more dispersed in the morning but more concentrated at night, which allows more airspace to satisfy the three-indicator constraints during the nighttime. The differences in Layer 4 are relatively minor, while Layer 7 and Layer 10 show almost no change.

Figure 15 shows the comparisons of preliminary feasible airspace between morning and evening. Left Y-axis represents proportions of each layer at different time, while right Y-axis shows the differences between morning and evening. Overall, there are no obvious differences between the two time periods for each layer. In Layer 1, the morning proportion is clearly lower than that at night. From Layer 2 to Layer 4, the morning proportion is slightly higher. From Layer 5 to Layer 8, the evening proportion becomes slightly higher. Layer 9 and Layer 10 are nearly the same. The differences between Layer 1 and Layer 2 rise sharply. It remains relatively stable in the middle layers and approaches zero both in Layer 9 and Layer 10, which indicates that the differences essentially vanish at higher altitudes.

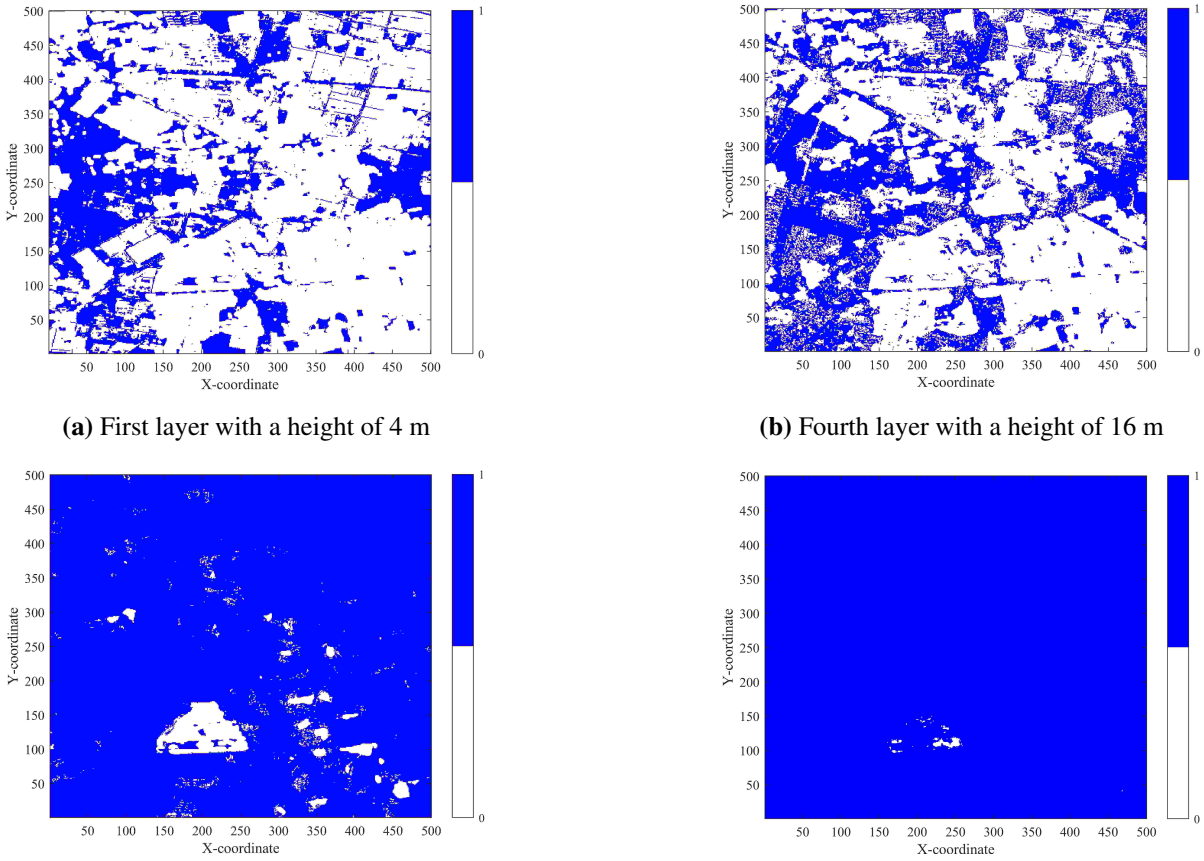

(a) First layer with a height of 4 m

(b) Fourth layer with a height of 16 m

(c) Seventh layer with a height of 28 m

(d) Tenth layer with a height of 40 m

Figure 14. Four layers of preliminary feasible airspace at 10 P.M.

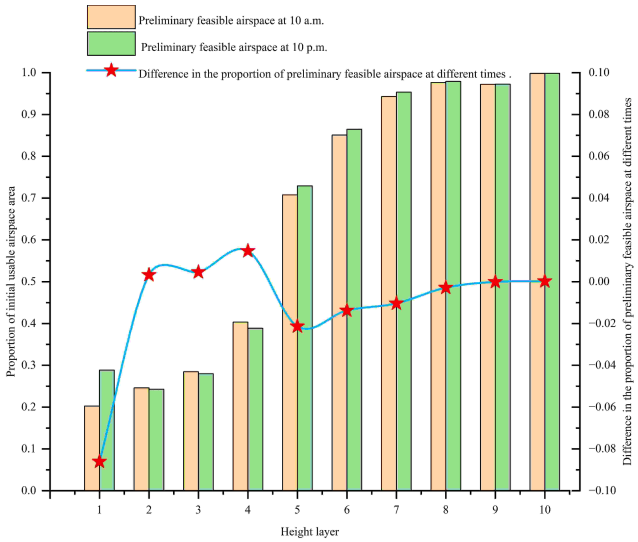

Figure 15. Proportions of preliminary feasible airspace at different times.

4.4. Results of Pareto ranking

A Pareto ranking is then applied to optimize the results of quadrant analysis based on Eq (3.31) and optimal airspace can be selected in terms of static risk, airspace availability, and dynamic risk. To save space, this parameter was also subjected to sensitivity analysis. Based on the results of the sensitivity analysis, the thresholds shown in Table 9 were obtained. A sorting was conducted at the time of 10:00 A.M. and 10:00 P.M. to obtain feasible airspace with a high quality, which provides support for the subsequent connectivity testing. By using a Pareto ranking for the results of a quadrant analysis at 10:00 A.M., the objective value of each voxel in urban airspace can be calculated, the top 70% of which are selected as the final feasible airspace. The results are given in Figure 16.

Table 9. Parameter settings for Pareto ranking.

Parameter	Value
w_1	0.4
w_2	0.4
w_3	0.2
$f_{\text{threshold}}$	0.8
$l_{\text{threshold}}$	0.8
$\alpha_{\text{threshold}}$	0.25

As shown in Figure 16, there are many infeasible areas in Layer 1 around $(0, 500)$, $(0, 0)$, $(300, 0)$, and $(500, 0)$ with few changes from Layer 1 to Layer 3. This indicates many significant restrictions in the lower altitude airspace. Starting from Layer 4, the feasible airspace near $(0, 0)$ expands a lot improving the suitability of mid-level airspace. As the altitude increases, the feasible airspace continues to expand from Layer 6 to Layer 10. Notably, Layer 10 is almost full of feasible airspace except for a few areas near $(400, 400)$.

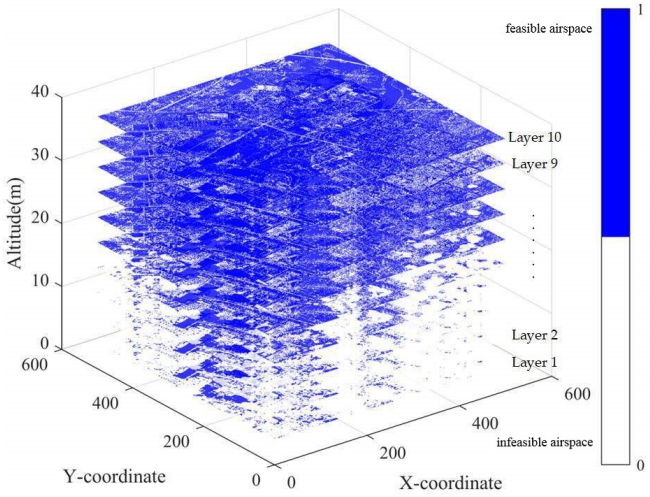

Figure 16. 3D final feasible airspace at 10:00 A.M.

Figure 17 presents four layers of final feasible airspace at 10:00 A.M., which are Layer 1, Layer 4, Layer 7, and Layer 10. The final feasible airspace of Layer 1 is only scattered in some regions such as $(100, 240)$, $(450, 250)$, and $(290, 450)$ with overall poor accessibility. In Layer 4, the feasible airspace expands significantly with more areas distributed around $(50, 50)$, $(100, 240)$, $(250, 250)$, $(290, 450)$, and $(450, 250)$. It is improved greatly compared to Layer 1 although still relatively scattered. In Layer 7, the feasible airspace exhibits a large and continuous distribution with only a few infeasible zones near $(200, 150)$, $(400, 100)$, and $(300, 400)$, which results in good overall connectivity. In Layer 10, almost no large infeasible areas remain and the airspace accessibility is the best. The few scattered infeasible zones are negligible.

Figure 18 illustrates the 3D final feasible airspace at 10 P.M., which is composed of ten layers. There is almost no final feasible airspace near $(0, 500)$, $(0, 0)$, $(200, 0)$, and $(500, 0)$ in Layer 1 with an overall low proportion. From Layer 1 to Layer 4, the changes are minimal and the infeasible airspace dominates in these layers. Starting from Layer 5, the large-scale feasible airspace starts appearing around $(0, 0)$ and $(0, 500)$. From Layer 6, feasible urban airspace in these regions gradually becomes dominant. In Layer 9, the infeasible zones mainly locate around $(0, 0)$ and $(250, 0)$ leading to a declined feasibility. In Layer 10, most of the airspace is feasible with only a few scattered infeasible spots presenting a pattern of feasibility as the main state with limited scattered infeasibility.

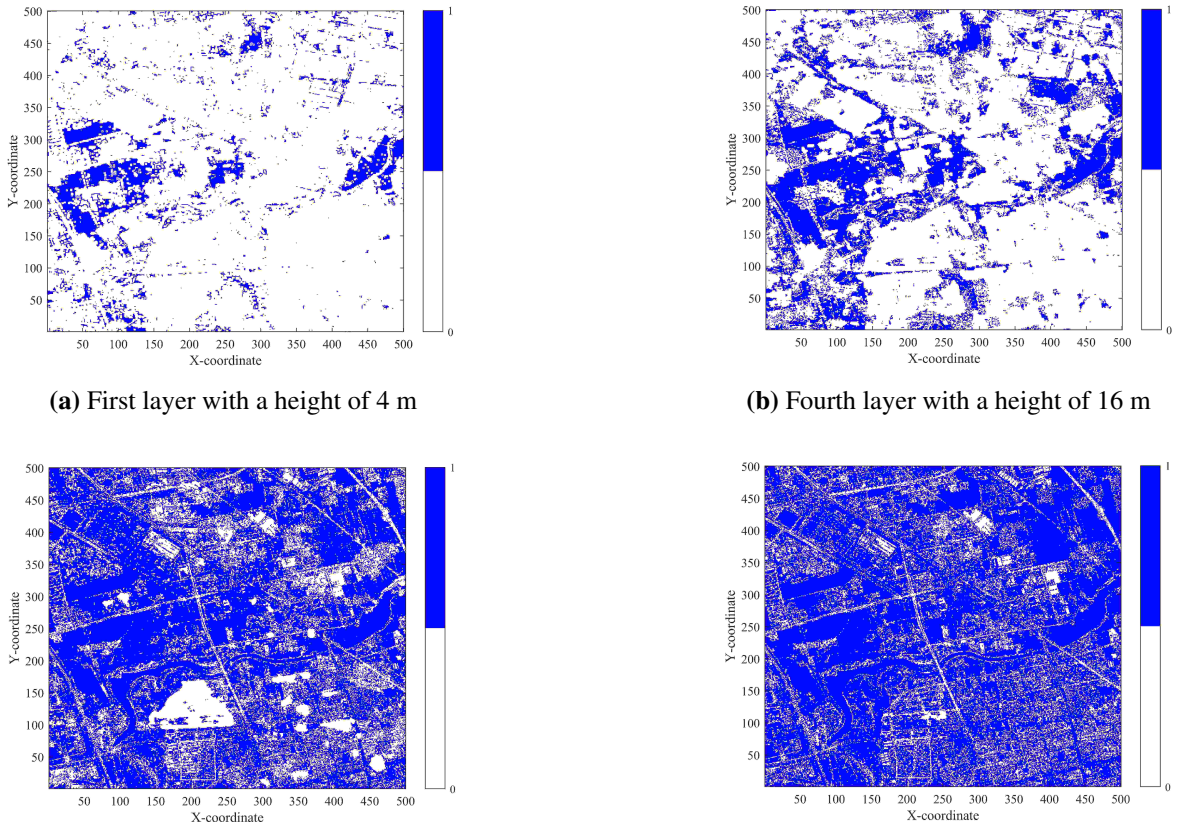

(a) First layer with a height of 4 m

(b) Fourth layer with a height of 16 m

(c) Seventh layer with a height of 28 m

(d) Tenth layer with a height of 40 m

Figure 17. Four layers of final feasible airspace at 10 A.M.

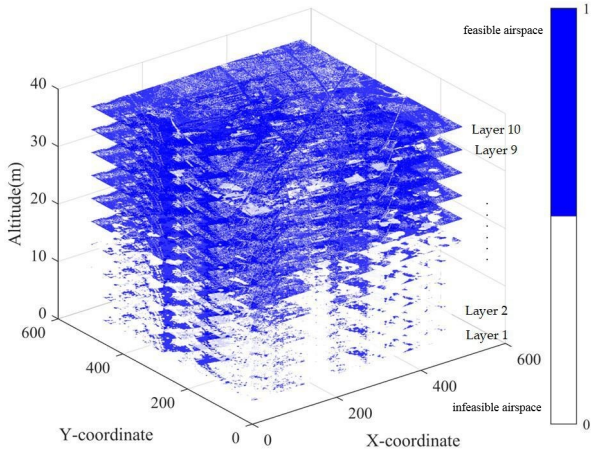

Figure 18. 3D final feasible airspace at 10:00 P.M.

As shown in Figure 19, the final feasible airspace is only sparsely distributed around $(100, 250)$ and $(500, 250)$ in Layer 1. In Layer 4, the feasible airspace expands with more feasible regions near $(300, 50)$ and $(100, 50)$. In Layer 7, the final feasible airspace increases significantly especially those locations around $(200, 125)$ and $(200, 375)$. The connectivity is improved a lot compared with lower layers. Nevertheless, some large infeasible airspace remains. In Layer 10, feasibility becomes optimal. A lot of infeasible airspace essentially disappears and only a few scatter somewhere in this layer.

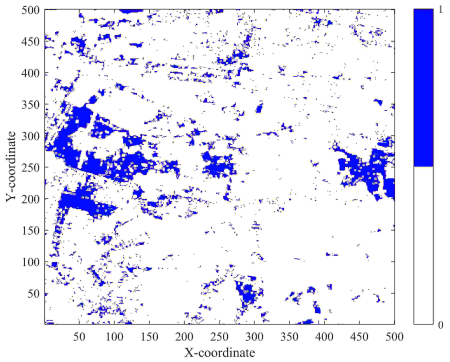

(a) First layer with a height of 4 m

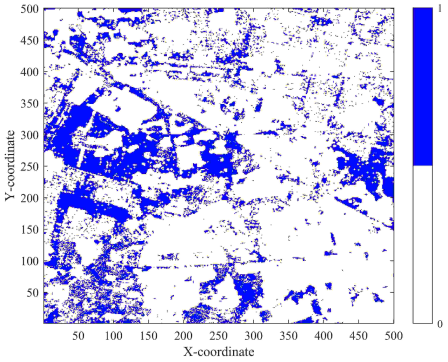

(b) Fourth layer with a height of 16 m

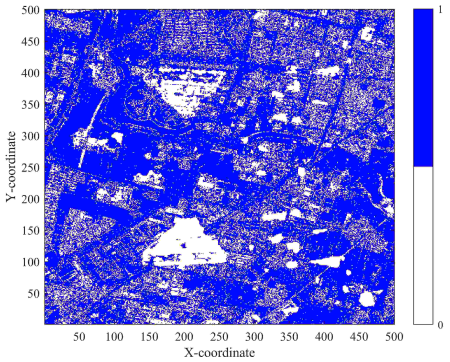

(c) Seventh layer with a height of 28 m

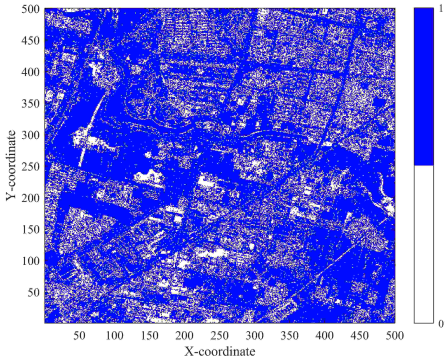

(d) Tenth layer with a height of 40 m

Figure 19. Four layers of the final feasible airspace at 10:00 P.M.

Figure 20 shows comparisons of final feasible airspace at different times across different layers. From Layer 1 to Layer 3, it remains nearly the same and Layer 4 is slightly higher in the morning than that in the evening. But from Layer 5 to Layer 8, it is higher in the evening than that in the morning. Layer 9 and Layer 10 show the opposite. According to the curve in the figure, Layer 1, Layer 2, and Layer 3 remain steady. Layer 3 and Layer 4 rise slightly. From Layer 4 to Layer 6, it drops sharply. From Layer 6 to Layer 10, it only fluctuates slightly. Layer 10 shows a difference of about 0.01, indicating that the two time periods would converge in higher layers.

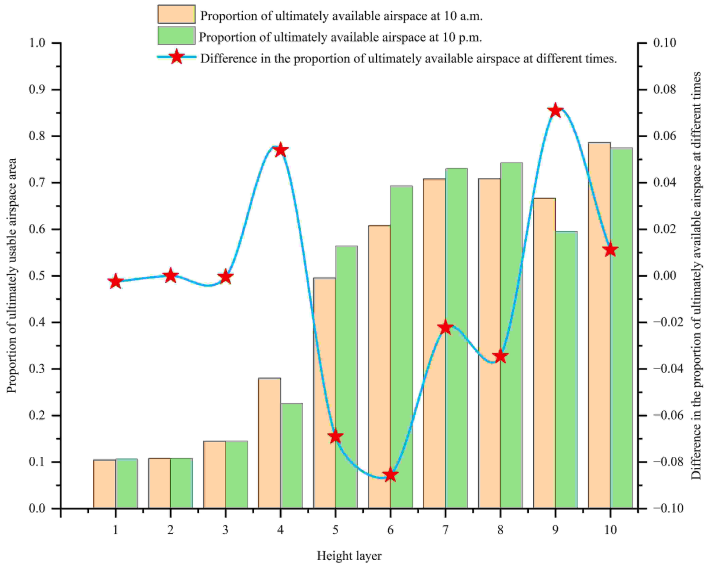

Figure 20. Comparisons of the final feasible airspace at different times.

5. Connectivity test of urban airspace

To further evaluate the practical usability of the final feasible airspace, a connectivity test was conducted using the Dijkstra algorithm. The purpose of this test is to examine whether a continuous path can be generated between the predefined starting point and destination point within each altitude layer. In this study, the connectivity test was performed independently for each altitude layer based on the final feasible airspace obtained after the improved Pareto ranking. The path-search process was conducted on a two-dimensional grid for each layer, where feasible voxels were treated as accessible nodes and infeasible voxels were treated as obstacles.

The computational complexity of the Dijkstra algorithm was also considered in the connectivity test. For a graph with V nodes and E edges, the time complexity of Dijkstra's algorithm depends on the data structure used for selecting the node with the minimum tentative distance. When a priority queue is used, the complexity is $O((V + E) \log V)$. In the MATLAB implementation used in this study, the node with the minimum tentative distance is selected through a direct search in the candidate queue. Therefore, the worst-case complexity is approximately $O(V^2 + E)$, which can be simplified as $O(V^2)$ for a regular grid graph where the number of edges is approximately linear with the number of nodes.

In this study, the complete urban airspace model contains $500 \times 500 \times 10$ voxels. However, the

connectivity test is conducted independently for each altitude layer rather than on the entire three-dimensional voxel space at once. Therefore, each search is performed on a two-dimensional grid with 500×500 nodes. The execution times of the layer-level connectivity tests are reported in Table 10. These results are used to evaluate the computational feasibility of the proposed connectivity test for offline strategic airspace evaluation.

Table 10. Execution time of layer-level connectivity tests using the Dijkstra algorithm.

Layer	10:00 A.M.		10:00 P.M.	
	Path length/m	Execution time/s	Path length/m	Execution time/s
Layer 1	No path	0.1929	No path	0.0674
Layer 2	No path	0.1856	No path	0.0438
Layer 3	No path	0.2233	No path	0.2795
Layer 4	No path	0.2965	No path	0.2018
Layer 5	No path	0.2661	No path	0.1053
Layer 6	No path	0.3022	7598.69	2.9937
Layer 7	7577.98	3.0569	7445.97	3.3101
Layer 8	7502.83	3.0062	7337.10	3.1653
Layer 9	No path	0.0111	7387.39	2.8236
Layer 10	7440.82	3.5588	7258.52	3.2754

As shown in Table 10, the execution time of each layer-level connectivity test is generally within a few seconds, indicating that the proposed layer-wise Dijkstra connectivity test is computationally manageable for offline urban airspace evaluation. In the 10:00 A.M. scenario, feasible paths are found in Layer 7, Layer 8, and Layer 10, while the lower layers do not provide continuous feasible paths between the starting point and destination point. In the 10:00 P.M. scenario, feasible paths are found from Layer 6 to Layer 10, suggesting that the nighttime feasible airspace has better connectivity in relatively higher altitude layers.

These results further confirm that higher-altitude layers generally provide better connectivity for UAV operations. Although the complete urban airspace model contains a large number of voxels, the layer-wise implementation avoids directly searching the entire three-dimensional voxel space and makes the connectivity test computationally feasible. For real-time airspace management applications, computational efficiency can be further improved through precomputed feasible-airspace maps, hierarchical graph abstraction, parallel layer-level search, or incremental path-search algorithms.

5.1. Risk-oriented connectivity test of urban airspace

To implement a risk-oriented connectivity test of urban airspace, the three weight coefficients w_1, w_2, and w_3 in the objective function should be set first. Higher values of w_1 and w_2 would focus on the static risk and dynamic risk, which are referred to as risk-oriented. The values of w_1, w_2, and w_3 are given in Table 11.

Table 11. Parameters for the risk-oriented connectivity test.

Parameter	Value
w_1	0.4
w_2	0.4
w_3	0.2

As shown in Figure 21, Layer 1, Layer 4, Layer 7, and Layer 10 are extracted. There are no suitable UAV paths from the starting point $(0, 500)$ to destination point $(500, 0)$ in Layer 1 and Layer 4. This means the connectivity of these two layers is relatively low and is associated with the proportions of the final feasible airspace. In Layer 7, there is a completely connected UAV path with a total length of 7578 m, which indicates high connectivity in this layer. The path length in Layer 10 is 7440.8 m, which is a little shorter than that of Layer 7. It is the best among the four layers. The connectivity of Layer 10 is the highest as well as having optimal path-planning efficiency. It can be concluded that the urban airspace within 28 m to 40 m at 10:00 A.M. proves a higher airworthiness.

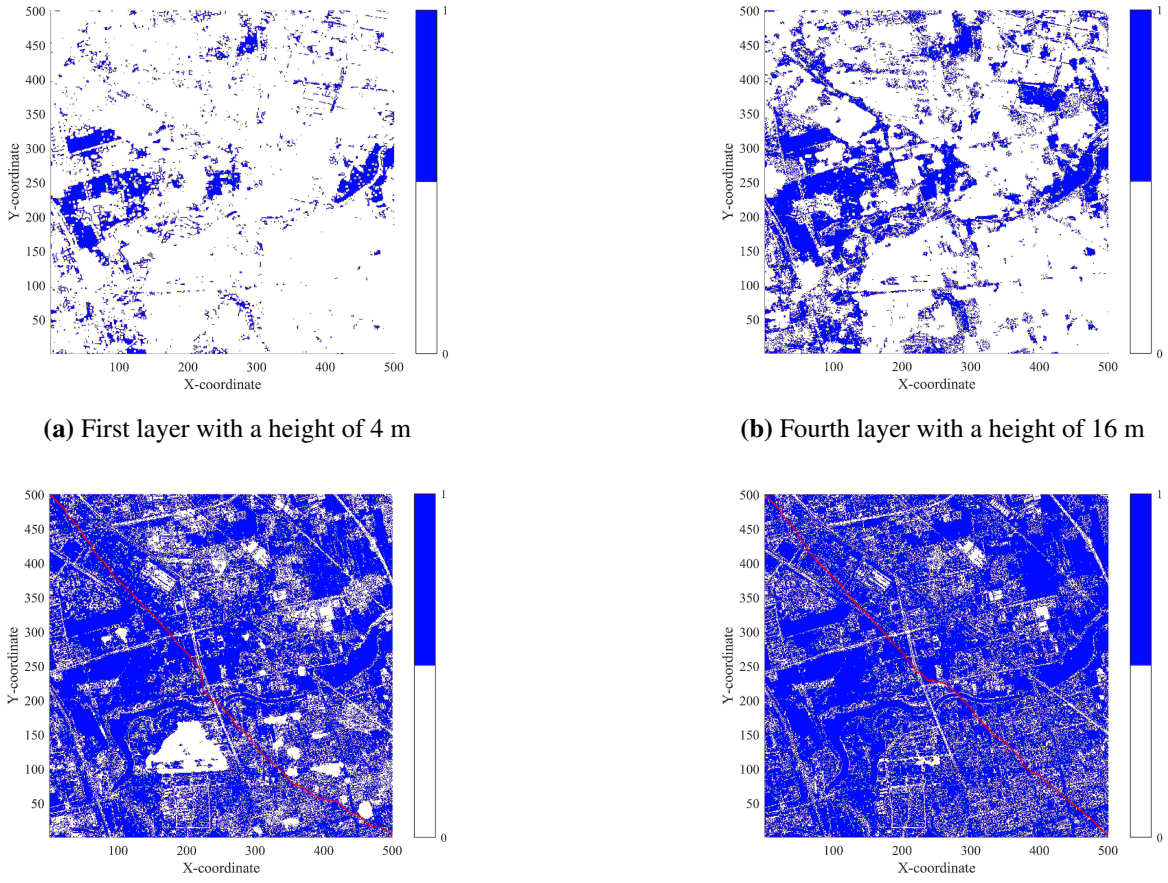

(a) First layer with a height of 4 m

(b) Fourth layer with a height of 16 m

(c) Seventh layer with a height of 28 m

(d) Tenth layer with a height of 40 m

Figure 21. Four layers of the risk-oriented connectivity test at 10:00 A.M.

Figure 22 shows the results of the risk-oriented connectivity test at 10:00 P.M. in four layers. At 10:00 P.M. in the figure, the connectivity of Layer 1 and Layer 4 remain relatively low and no connected UAV path can be established from a starting point $(0, 500)$ to a destination point $(500, 0)$, which is

consistent with the results at 10:00 A.M. In Layer 7, a UAV path can be generated with a length of 7446 m and is shorter than the path in this layer at 10:00 A.M. (7578 m). That is because the proportion of feasible airspace at 10:00 P.M. in Layer 7 is higher and there are more available waypoints for UAVs at night. The length of the UAV's path in Layer 10 is reduced to 7258.5 m, , which is the shortest among all the nighttime layers. Layer 10 exhibits the best connectivity indicating a more favorable airspace in this layer.

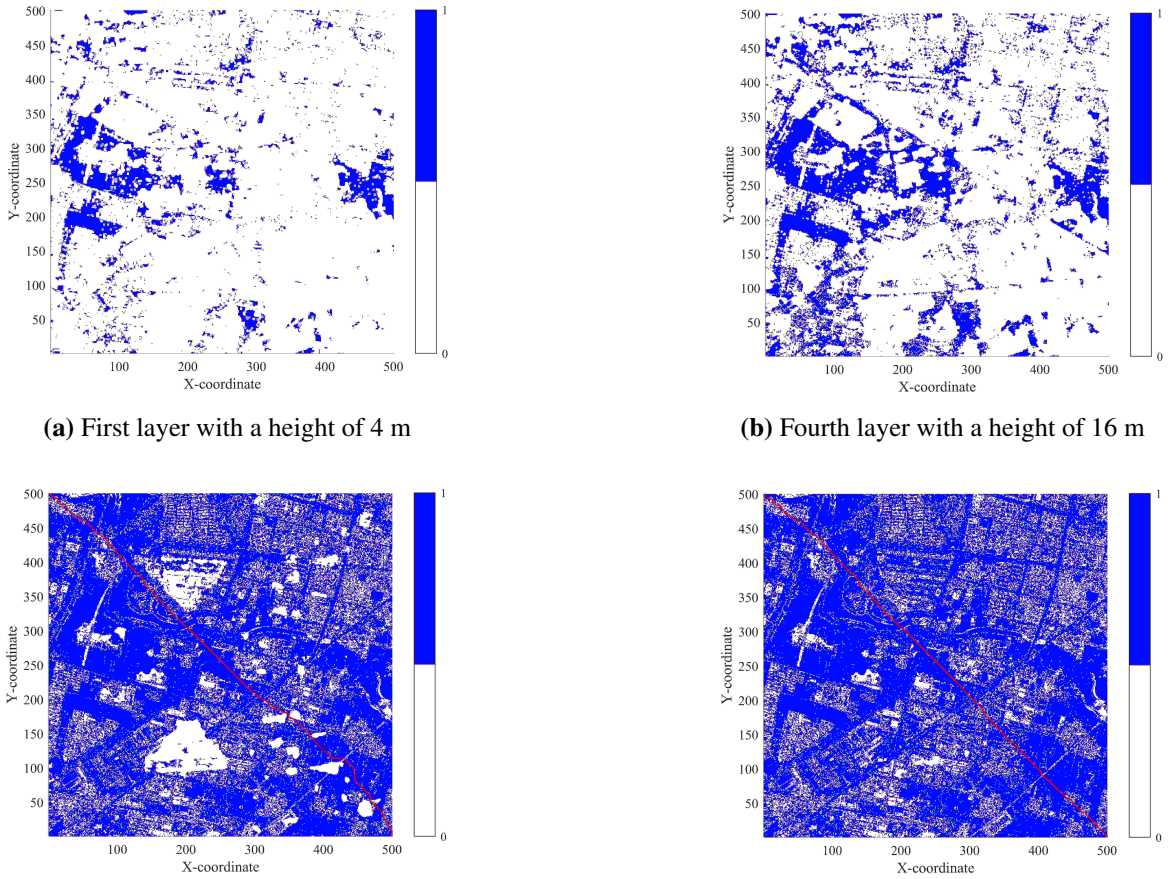

(a) First layer with a height of 4 m

(b) Fourth layer with a height of 16 m

(c) Seventh layer with a height of 28 m

(d) Tenth layer with a height of 40 m

Figure 22. Four layers of risk-oriented connectivity test at 10:00 P.M.

Overall, the risk-oriented connectivity test demonstrates that the urban airspace connectivity at 10:00 P.M. is generally superior to that at 10:00 A.M., where the connectivity is improved significantly as altitude increases. The higher urban airspace at nighttime not only offers a more stable structure but also stronger connectivity, making it more suitable for safe UAV operations.

5.2. Availability-oriented connectivity test of urban airspace

As analyzed previously, when w_3 is higher, the urban airspace availability becomes the focus accordingly. The values of w_1, w_2, and w_3 are given in Table 12.

Table 12. Parameters for the availability-oriented connectivity test.

Parameter	Value
w_1	0.2
w_2	0.2
w_3	0.6

The availability-oriented connectivity tests at 10:00 A.M. in Layer 1, Layer 4, Layer 7, and Layer 10 are given in Figure 23. The infeasible airspace still dominates in Layer 1 and Layer 4, which leads to no continuous UAV path from the starting point (0, 500) to the destination point (500, 0). Generally, it is consistent with the results of the risk-oriented test. When the altitude increases, the coverage of the final feasible airspace in Layer 7 expands significantly enabling a construction of the shortest UAV path with a length of 7484.3 m. It is a little shorter than the length of 7578 m observed in the risk-oriented test indicating the availability-oriented strategy could provide better connectivity at this height. In Layer 10, the airspace connectivity is further improved with a path length of 7440.8 m, which is identical to that of the risk-oriented test. In this way, both of the two strategies yield similar connectivity at higher layers.

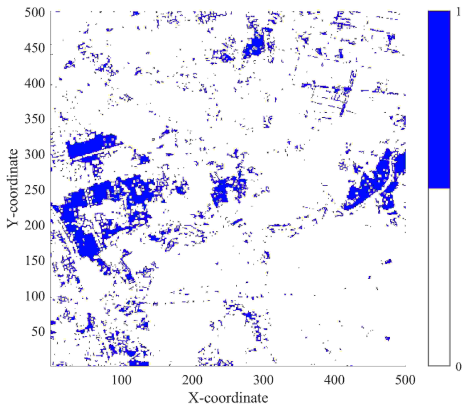

(a) First layer with a height of 4 m

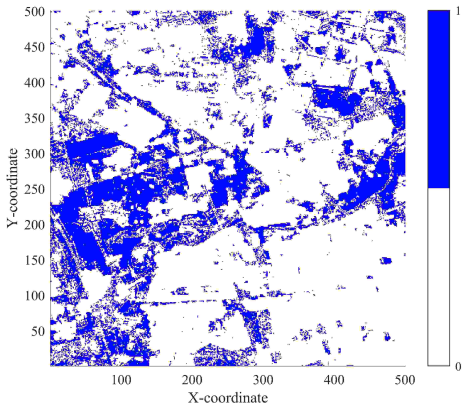

(b) Fourth layer with a height of 16 m

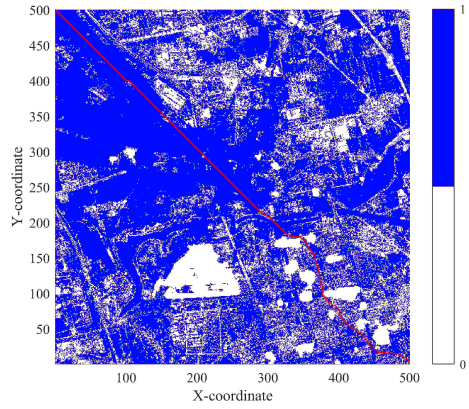

(c) Seventh layer with a height of 28 m

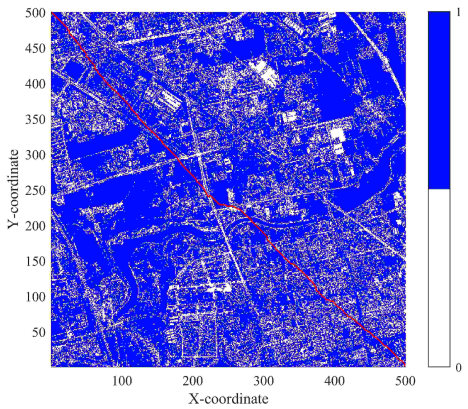

(d) Tenth layer with a height of 40 m

Figure 23. Four layers of the availability-oriented connectivity test at 10:00 A.M.

Similarly, the results of the availability-oriented airspace connectivity test at 10:00 P.M. are given in Figure 24. There is still a lot of infeasible airspace in Layer 1 and Layer 4, which lead to no connected UAV path from the starting point to the destination point. In Layer 7, there exists a connected UAV path with the shortest path length of 7440.1 m. However, compared with the results at 10:00 A.M., the UAV's path at night is noticeably shorter. In Layer 10, the path length is 7258.5 m, which is significantly shorter than 7440.8 m that is obtained in the availability-oriented connectivity test at 10:00 A.M. It further confirms that high-altitude layers in urban airspace at 10:00 P.M., particularly Layer 10, outperform the conditions at 10:00 A.M. in terms of airspace connectivity.

In summary, nighttime high-altitude airspace (e.g., Layer 7 and Layer 10) demonstrates superior connectivity. Among these, Layer 10 consistently yields the shortest UAV path across all scenarios, which proves that nighttime high-altitude airspace is more suitable for safe and efficient UAV operations.

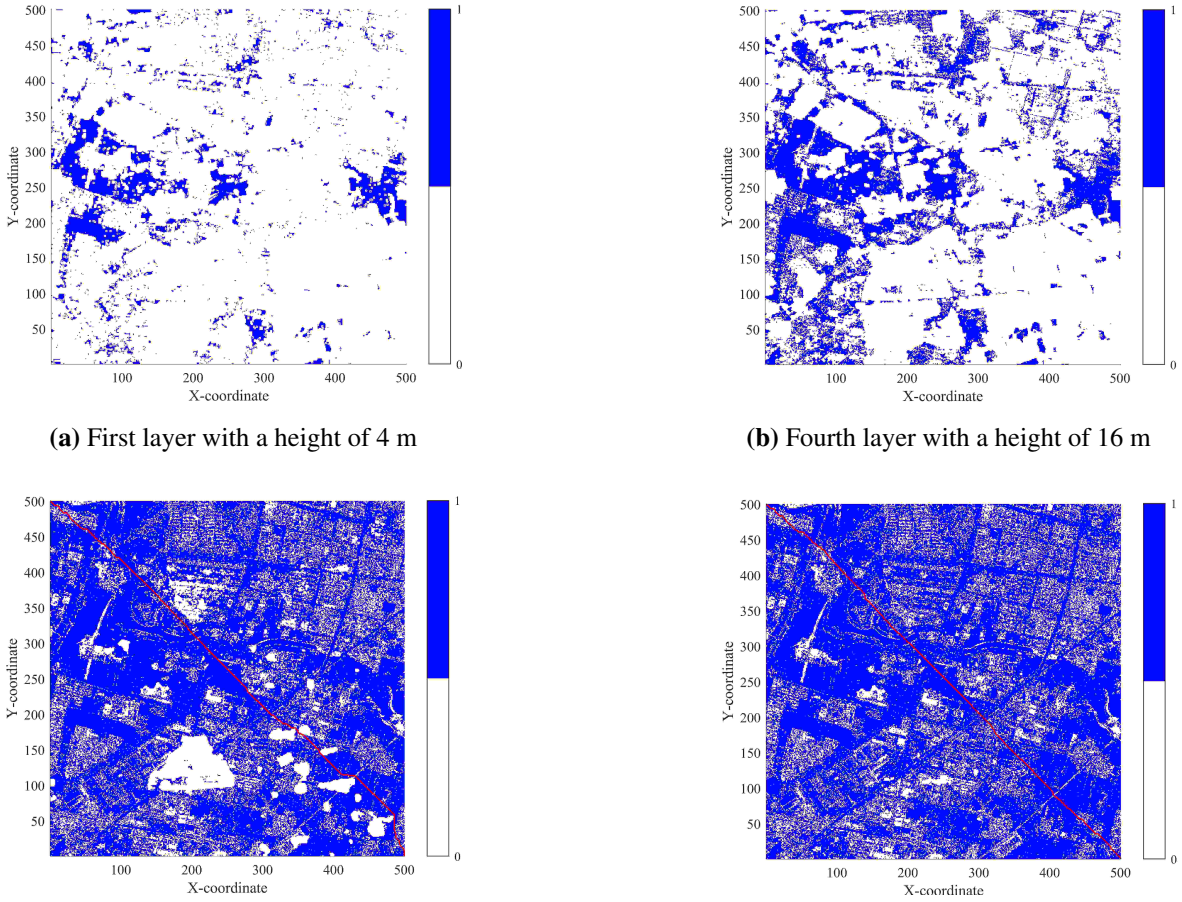

(a) First layer with a height of 4 m

(b) Fourth layer with a height of 16 m

(c) Seventh layer with a height of 28 m

(d) Tenth layer with a height of 40 m

Figure 24. Four layers of availability-oriented connectivity test at 10:00 P.M.

6. Conclusions

This paper proposes a quantitative evaluation framework for urban low-altitude airspace by integrating airspace availability, static risk, and dynamic risk. First, a voxel-based method is used

to quantify airspace availability. Then, multi-risk models are constructed to evaluate static risk and dynamic risk. Based on these indicators, quadrant analysis is applied to identify preliminary feasible airspace, and an improved Pareto-ranking method is further used to obtain the final feasible airspace distribution. Using real GIS data from Changqing District, Jinan City, a high-resolution 3D urban airspace model below 40 m is constructed and evaluated at 10:00 A.M. and 10:00 P.M. The results show that airspace feasibility and connectivity generally improve with increasing altitude. In particular, the airspace between 28 m and 40 m provides better connectivity, and the connectivity at 10:00 P.M. is generally superior to that at 10:00 A.M. The proposed method also has practical engineering value for UAV route planning, low-altitude airspace management, operation authorization, and risk control. The generated feasible airspace maps can be used as spatial constraints or risk-aware cost maps for UAV route planning. The layer-based evaluation results can help identify suitable flight layers and provide quantitative evidence for airspace management and pre-flight authorization. In addition, the integration of static and dynamic risks can help identify high-risk areas and time-varying population exposure, thereby supporting targeted risk mitigation before UAV operations.

Although this study focuses on a specific urban area, the proposed framework can be extended to other regions by adjusting input data and parameter settings according to local building distribution, population distribution, and operational requirements. It should be noted that the thresholds and parameters used in this study may need to be recalibrated for cities with different urban morphologies, building densities, road-network structures, and population activity patterns. In addition, different national or regional UAV regulations, such as altitude restrictions, no-fly zones, safety buffer requirements, and operational authorization rules, can be incorporated as additional spatial constraints or risk layers. Future work will further validate the proposed framework under different urban forms, regulatory contexts, and UAV operation scenarios.

Author contributions

Hao Li: Paper writing and overall coordination; Hua Wu: Conceptualization; Yang Liu: Project management and paper revision; HaiLong Dong: Investigation; HuaYu Liu: Data management; Shuai Fan: Visualization. All authors have read and approved the final version of the manuscript for publication.

Use of Generative-AI tools declaration

The authors declare they have not used Artificial Intelligence (AI) tools in the creation of this paper.

Acknowledgements

The authors would like to thank the Shandong Province Higher Education Schools' Youth Innovation Teams Development Program, Shandong Province's Science and Technology SMEs Innovation Ability Enhancement Project, and the Ministry of Education's Intelligent Air-Ground Integration Vehicle and Control Engineering Research Center (Xihua University) for the funding of open research topics, Jinan "Solving Problems by Tendering for Champions" Program.

Funding

This research was funded by the Jinan "Solving Problems by Tendering for Champions" Program (Grant Number 202527022), Shandong Provincial Higher School Youth Innovation Team Development Program (Grant Number 2022KJ318), and Shandong Provincial Science and Technology SMES Innovation Ability Improvement Project (Grant Number 2023TSGC0229).

Conflict of interest

The authors declare no conflicts of interest.

Data availability statement

The datasets generated and analyzed during the current study are available from the corresponding author, Dr. Yang Liu (liuyang@sdjtu.edu.cn), upon reasonable request.

References

1. R. Y. Liu, H. L. Kang, R. Bao, S. Y. Gong, Y. F. Yao, Y. Wu, An improved aphid optimization algorithm with soft thresholding, *AIMS Math.*, **11** (2026), 3534–3559. https://doi.org/10.3934/math.2026144
2. Q. M. Li, Y. H. Yan, S. H. Lan, FCA-YOLO: a small object detection method based on feature attention fusion for UAV remote sensing images, *AIMS Math.*, **11** (2026), 5172–5191. https://doi.org/10.3934/math.2026211
3. X. T. Sun, Y. Hu, Y. C. Qin, Y. Zhang, Risk assessment of unmanned aerial vehicle accidents based on data-driven Bayesian networks, *Reliab. Eng. Syst. Safety*, **248** (2024), 110185. https://doi.org/10.1016/j.ress.2024.110185
4. S. Oh, Y. Yoon, Urban drone operations: a data-centric and comprehensive assessment of urban airspace with a Pareto-based approach, *Transp. Res. Part A Policy Pract.*, **182** (2024), 104034. https://doi.org/10.1016/j.tra.2024.104034
5. J. Yang, Y. J. Wang, X. Hang, D. Delahaye, A review on airspace design and risk assessment for urban air mobility, *IEEE Access*, **12** (2024), 157599–157611. https://doi.org/10.1109/access.2024.3481148
6. L. Davies, Y. Vagapov, V. Grout, S. Cunningham, A. Anuchin, Review of air traffic management systems for UAV integration into urban airspace, In: *2021 28th International Workshop on Electric Drives: Improving Reliability of Electric Drives (IWED)*, Moscow, Russia, 2021, 1–6. https://doi.org/10.1109/iwed52055.2021.9376343
7. M. Doole, J. Ellerbroek, V. L. Knoop, J. M. Hoekstra, Constrained urban airspace design for large-scale drone-based delivery traffic, *Aerospace*, **8** (2021), 38. https://doi.org/10.3390/aerospace8020038
8. C. C. Xu, X. H. Liao, J. M. Tan, H. P. Ye, H. Y. Lu, Recent research progress of unmanned aerial vehicle regulation policies and technologies in urban low altitude, *IEEE Access*, **8** (2020), 74175–74194. https://doi.org/10.1109/access.2020.2987622

9. S. Bae, H. S. Shin, A. Tsourdos, Structured urban airspace capacity analysis: four drone delivery cases, *Appl. Sci.*, **13** (2023), 3833. https://doi.org/10.3390/app13063833
10. U. J. Lee, S. J. Ahn, D. Y. Choi, S. M. Chin, D. S. Jang, Airspace designs and operations for UAS traffic management at low altitude, *Aerospace*, **10** (2023), 737. https://doi.org/10.3390/aerospace10090737
11. W. Z. Zhang, H. Wu, Y. Liu, S. Y. Zhou, H. L. Dong, H. Y. Liu, Dual-metric-based assessment and topology generation of urban airspace with quadrant analysis and Pareto ranking, *Aerospace*, **11** (2024), 978. https://doi.org/10.3390/aerospace11120978
12. S. Oh, Y. Yoon, Data-driven risk analysis of unmanned aircraft system operations considering spatiotemporal characteristics of population distribution, *Transp. Res. Interd. Perspect.*, **16** (2022), 100732. https://doi.org/10.1016/j.trip.2022.100732
13. Y. W. Sun, H. F. Tao, V. Stojanovic, Open-set classification method via latent representation prompt and time-frequency fusion toward unknown fault recognition, *Adv. Eng. Inform.*, **68** (2025), 103779. https://doi.org/10.1016/j.aei.2025.103779
14. Y. W. Sun, H. F. Tao, V. Stojanovic, Multi-domain weakly decoupled domain generalization network for fault diagnosis under unknown operating conditions, *Knowl. Based Syst.*, **330** (2025), 114452. https://doi.org/10.1016/j.knosys.2025.114452
15. C. B. Qin, X. T. Ran, D. H. Zhang, Unsupervised image stitching based on generative adversarial networks and feature frequency awareness algorithm, *Appl. Soft Comput.*, **183** (2025), 113466. https://doi.org/10.1016/j.asoc.2025.113466
16. C. B. Qin, X. T. Ran, Efficient unsupervised image stitching using attention mechanism with deep homography estimation, *Comput. Mater. Continua*, **79** (2024), 1319–1334. https://doi.org/10.32604/cmc.2024.048850
17. E. Aldao, F. Veiga-López, C. P. C. Chanel, Y. Watanabe, H. González-Jorge, Dynamic UAV trajectory optimisation for parcel delivery with integrated third-party risk mitigation, *Reliab. Eng. Syst. Safety*, **262** (2025), 111178. https://doi.org/10.1016/j.ress.2025.111178
18. S. Y. Zhou, Y. Liu, X. J. Zhang, H. L. Dong, W. Zhang, H. Z. Wu, et al., Risk assessment and distribution estimation for UAV operations with accurate ground feature extraction based on a multi-layer method in urban areas, *Drones*, **8** (2024), 399. https://doi.org/10.3390/drones8080399
19. V. C. Martinez, H. S. Shin, A. Tsourdos, Risk assessment for sUAS in urban environments: a comprehensive analysis, modelling and validation for safe operations, In: *AIAA SCITECH 2024 Forum*, 2024, Orlando 0232. https://doi.org/10.2514/6.2024-0232
20. A. S. Alatawi, A. A. Youssef, M. Abaza, R. Mesleh, F. S. Almehmadi, Evaluation of the feasibility of FSO/UAV communications in NEOM smart city, *Results Eng.*, **26** (2025), 105256. https://doi.org/10.1016/j.rineng.2025.105256
21. S. Huang, J. P. Shi, Q. Zhu, Z. H. Du, Y. X. Lyu, Z. Liu, Multiple UAVs cooperatively circumnavigating a group of non-cooperative targets in a GPS-free environment via a range-only distributed controller, *Aerosp. Sci. Technol.*, **158** (2025), 109924. https://doi.org/10.1016/j.ast.2024.109924

22. H. Wu, H. B. Duan, Hierarchical pigeon inspired optimization based Multi-UAV obstacle avoidance control, *Aerosp. Sci. Technol.*, **159** (2025), 109963. https://doi.org/10.1016/j.ast.2025.109963
23. H. Y. Tang, Q. Zhu, B. Qin, R. Y. Song, Z. Li, UAV path planning based on third-party risk modeling, *Sci. Rep.*, **13** (2023), 22259. https://doi.org/10.1038/s41598-023-49396-4
24. Civil Aviation Safety Authority, *Potential damage assessment of a mid-air collision with a small UAV*, Technical Report, 2013.
25. Q. Y. Li, Q. G. Wu, H. Y. Tu, J. P. Zhang, X. Zou, S. Huang, Ground risk assessment for unmanned aircraft focusing on multiple risk sources in urban environments, *Processes*, **11** (2023), 542. https://doi.org/10.3390/pr11020542
26. B. Z. Pang, X. T. Hu, W. Dai, K. H. Low, UAV path optimization with an integrated cost assessment model considering third-party risks in metropolitan environments, *Reliab. Eng. Syst. Safety*, **222** (2022), 108399. https://doi.org/10.1016/j.ress.2022.108399
27. X. T. Hu, B. Z. Pang, F. Q. Dai, K. H. Low, Risk assessment model for UAV cost-effective path planning in urban environments, *IEEE Access*, **8** (2020), 150162–150173. https://doi.org/10.1109/access.2020.3016118
28. C. H. Koh, K. H. Low, L. Li, Y. Zhao, C. Deng, S. K. Tan, et al., Weight threshold estimation of falling UAVs (unmanned aerial vehicles) based on impact energy, *Transp. Res. Part C Emerging Technol.*, **93** (2018), 228–255. https://doi.org/10.1016/j.trc.2018.04.021
29. S. Bertrand, N. Raballand, F. Viguier, Evaluating ground risk for road networks induced by UAV operations, In: *2018 International Conference on Unmanned Aircraft Systems (ICUAS)*, Dallas, 2018, 168–176. https://doi.org/10.1109/icuas.2018.8453441
30. W. N. Alexander, J. Whelchel, Flyover noise of multi-rotor sUAS, In: *Inter-Noise and Noise-Con Congress and Conference Proceedings*, Madrid, 2019, 2548–2558.